Two distinct modes of hemodynamic responses across the human cortex

Samira M. Epp[1,2,3], Gabriel Castrillón[1,2,4], Beijia Yuan[5], Jessica Andrews-Hanna[6,7], Christine Preibisch[2,8], Valentin Riedl[1,2]

[1]*Friedrich-Alexander-University, Department of Neuroradiology, Erlangen, Germany*
[2]*Technical University of Munich, School of Medicine and Health, Institute of Neuroradiology, Munich, Germany*
[3]*Ludwig-Maximilians-University, Graduate School of Systemic Neurosciences, Munich, Germany*
[4]*Research Group in Medical Imaging, SURA Ayudas Diagnósticas, Medellin, Colombia*
[5]*University of California, Department of Physics, San Diego, California, USA*
[6]*University of Arizona, Department of Psychology, Tucson, AZ, USA*
[7]*University of Arizona, Cognitive Science, Tucson, AZ USA*
[8]*Technical University of Munich, School of Medicine and Health, Clinic for Neurology, Munich, Germany*

ABSTRACT

Functional magnetic resonance imaging (fMRI) detects changes in brain activity by measuring fluctuations in blood oxygenation. The interpretation of the blood-oxygenation-level-dependent (BOLD) fMRI signal relies on the mechanism of neurovascular coupling, which closely links changes in neuronal activity to changes in cerebral blood flow (ΔCBF). Whether uniform neurovascular coupling applies to the entire human cortex is yet to be proven. We used BOLD fMRI along with quantitative fMRI to assess the cerebral metabolic rate of oxygen (CMRO2) associated with both positive and negative BOLD signal changes (ΔBOLD) using various task and baseline conditions. Contrary to conventional BOLD signal interpretations, we found decreases in CMRO2 in 12-40% of voxels with significant positive ΔBOLD and increases in CMRO2 in 40-66% of voxels with significant negative ΔBOLD, such as in the default mode network. This indicates a substantial number of discordant voxels where the sign of BOLD signal changes is contrary to the underlying metabolic activity. We identified differences in neurovascular coupling in these discordant voxels during both baseline and task states. During baseline, these voxels showed a lower oxygen extraction fraction (OEF) and CMRO2 compared to concordant voxels. In task states, oxygen demand in discordant voxels was primarily regulated via ΔOEF (58%), whereas in concordant voxels, ΔCBF (87%) was the primary regulatory mechanism. Thus, we propose ΔOEF as a complementary mechanism to ΔCBF in regulating oxygen demand across the human cortex. In summary, the canonical interpretation of positive and negative BOLD signal changes in terms of increased or decreased neural activity might be misleading, and we recommend quantitative fMRI or additional CBF measurements for a more valid interpretation of regional BOLD signal changes in relation to neuronal activity.

INTRODUCTION

Neuronal activity constitutes the principal energy expenditure of the brain, quantified as the cerebral metabolic rate of oxygen (CMRO2) (Engl & Attwell, 2015). Functional magnetic resonance imaging (fMRI) is a powerful and non-invasive method to localize brain activity during perception and cognition in the cortex of humans and other species (S.-G. Kim & Ogawa, 2012). However, the fMRI signal does not directly measure oxygen metabolism. Instead, it detects changes in blood oxygenation, which is why it is called the blood-oxygenation-level-dependent (BOLD) signal. Changes in the BOLD signal (ΔBOLD) due to a task are interpreted as local changes in neuronal activity. This interpretation is based on the well-known mechanism of neurovascular coupling, which links changes in neuronal activity to changes in cerebral blood flow (CBF) (Attwell et al., 2010; Drew, 2022; Hall et al., 2016; Hillman, 2014; Howarth et al., 2021; Leithner & Royl, 2014; Phillips et al., 2016).

Early studies of the human visual cortex using positron emission tomography (PET) have shown that a modest increase in CMRO2 due to visual stimulation is accompanied by a much larger increase in CBF (Fox et al., 1988; Fox & Raichle, 1986). A positive ratio of ΔCBF/ΔCMRO2 (*n*-ratio) of approximately 2-4 is the basis of the hemodynamic response model, which allows the interpretation of a positive BOLD response as increased neuronal activity and vice versa (Ances et al., 2008; Buxton, 2010; Uludağ et al., 2004). In this manuscript, we use the term 'canonical hemodynamic response' for *n*-ratios > 1. Although the regulatory mechanisms of a canonical response are still debated (A. D. Ekstrom, 2021; Hillman, 2014), it is commonly assumed that a surplus increase in CBF maintains a high partial pressure of oxygen in capillaries to facilitate oxygen diffusion into brain tissue (Buxton, 2020, 2023; DiNuzzo et al., 2023).

At the mesoscopic level, research groups have validated the connection between increased neural spiking or synaptic activity and increased CBF or BOLD signals (Boorman et al., 2010; Devor et al., 2003; Gagnon et al., 2015; Logothetis et al., 2001; Siero et al., 2013). Further studies have demonstrated a direct relationship between incoming spiking activity and positive BOLD signal changes when controlling for the extent of sensory input (Heeger et al., 2000; D. S. F. Hyder et al., 2010; Rees et al., 2000; Vanzetta & Grinvald, 1999). Similarly, decreased neuronal activity or inhibitory processes were associated with negative BOLD signal changes (Devor et al., 2007; Fracasso et al., 2022, S. 20; Mullinger et al., 2014; Pasley et al., 2007; Shmuel et al., 2002, 2006; Stefanovic et al., 2004; Wilson et al., 2019). Combined, these studies support the interpretation of BOLD signal changes as localized changes in neuronal activity within fMRI voxels. However, there is an ongoing debate on how well these findings, obtained primarily from sensory cortices, generalize to the rest of the cortex, particularly in humans.

Several studies have questioned that BOLD signal changes are consistently related to neuronal activity. For instance, animal experiments involving pharmacological interventions demonstrated that both CBF and metabolic activity can exhibit significant task-induced

changes, often with minimal or substantially reduced corresponding changes in BOLD signals (Leithner et al., 2010; Zaldivar et al., 2014). This suggests a decoupling of the hemodynamic response from neuronal activity under certain conditions (Drew, 2019, 2022; Rossetti et al., 2021). This uncoupling is supported by studies showing no change or even increased metabolism despite significant negative ΔBOLD or ΔCBF (Devor et al., 2008; Martínez-Maestro et al., 2019; Nagaoka et al., 2006; Stiernman et al., 2021). In human imaging, matters are further complicated because the BOLD signal from macroscopic fMRI voxels is a complex amalgamation of microscopic alterations in CBF, cerebral blood volume (CBV), and the oxygen extraction fraction (OEF) during capillary passage (Buxton, 2010; Buxton & Frank, 1997; D. S. F. Hyder, 2010). Moreover, a varying vasculature across brain regions might induce different BOLD signal amplitudes (Shaw et al., 2021). Finally, various neurochemical processes, beyond direct neuronal activity, are known to modulate the BOLD signal (Boynton, 2011; Cardoso et al., 2012; Das & Sirotin, 2011; A. Ekstrom, 2010; Sirotin & Das, 2009; Tsvetanov et al., 2020).

Together, these studies indicate that different hemodynamic mechanisms can lead to similar macroscopic BOLD signal changes. Moreover, despite substantial evidence for a canonical hemodynamic response in sensory and motor cortices, it is well known that the *n*-ratio varies across the human cortex. Several studies have shown regional differences in hemodynamic responses, especially between cortical and subcortical regions (Bergel et al., 2020; Devonshire et al., 2012; Roy et al., 2021; Sanganahalli et al., 2016; Schridde et al., 2008; Shaw et al., 2021; Shih et al., 2011). Finally, it is well known that hemodynamics and vasculature are impaired in certain brain disorders, possibly impacting the comparison of BOLD signal patterns between patients and healthy controls (Buxton, 2010; Fleisher et al., 2009). Together, these observations cast doubt on whether the amplitude and sign of the BOLD signal response reliably indicate changes in neuronal activity across the entire cortex.

This question can be addressed by measuring the absolute metabolic activity underlying positive and negative BOLD signal changes. While the gold standard for CBF and CMRO2 measurements is ^{15}O PET, this technique requires an on-site cyclotron, a sophisticated imaging setup, and significant experience in performing multiple experiments within the same individual using three different radiotracers (e.g., CBF: 15O-water, CBV: 15O-CO, OEF: 15O-gas) of short half-lives (Fox & Raichle, 1986; F. Hyder et al., 2016; Ito et al., 2021). Furthermore, this methodology is invasive and poses significant demands on participants owing to the exposure to radioactivity and the requirement for arterial sampling. As an alternative, various MRI approaches have been developed over the past three decades to accurately quantify (changes in) oxygen metabolism using either gas calibration (Chiarelli et al., 2007; Davis et al., 1998; Germuska et al., 2019), R2'-calibration (Blockley et al., 2012; Chen et al., 2022a), or quantitative susceptibility mapping (Fan et al., 2014; Haacke et al., 2010; Xu et al., 2014). In addition, the quantitative BOLD (qBOLD) approach is based on an analytical model (Yablonskiy & Haacke, 1994) that relates R2' to OEF (An & Lin, 2000; He et al., 2008; He & Yablonskiy, 2007; Stone & Blockley, 2017a). For recent reviews, see (Alzaidi et al., 2024; Jiang & Lu, 2022). A multiparametric variant of the qBOLD technique (mqBOLD) combines separate measurements

of the intrinsic and effective relaxation times, T2 and T2* for R2', with an independent quantification of CBV for OEF measurement (Alzaidi et al., 2024; Christen et al., 2012; Hirsch et al., 2014; Kaczmarz, Hyder, et al., 2020; Stone & Blockley, 2017b). The mq-BOLD technique has been widely applied to study patient groups with vascular pathologies and brain tumors, in our lab (Gersing et al., 2015; Göttler et al., 2019; Kaczmarz et al., 2021; Kufer et al., 2022; Preibisch et al., 2017; Tóth et al., 2013; Wiestler et al., 2016) as well as by others, e.g. (Bouvier et al., 2015; Maralani et al., 2018; Stadlbauer et al., 2017), summarized recently by (Alzaidi et al., 2024).

In this study, we applied the mqBOLD technique, including pseudo-continuous arterial spin labeling (pCASL) for CBF mapping, to healthy subjects and investigated changes in oxygen metabolism in relation to task-induced positive and negative ΔBOLD. Given the heterogeneous vascular composition of macroscale voxels and the diversity of mechanisms influencing the hemodynamic response, we hypothesized that ΔBOLD does not consistently reflect changes in oxygen metabolism across the cortex.

RESULTS

We obtained brain imaging data using BOLD and mqBOLD fMRI while participants carried out four distinct experimental conditions within the same imaging session (Figure 1A & 1B). These four conditions enabled us to identify (1) 'task-positive' regions exhibiting an increase in the BOLD signal, as well as (2) 'task-negative' regions with a negative BOLD response when participants performed a calculation task (CALC). Furthermore, we aimed for (3) positive BOLD responses in the same regions of the 'task-negative' contrast by employing an autobiographical memory task (MEM). We calculated contrast images for the two tasks (CALC, MEM) compared to either a low-level control task (CTRL) or an uncontrolled resting state (REST).

Quantitative fMRI, i.e., mqBOLD combined with pCASL MRI, measures CMRO2 as a metabolic proxy of neuronal activity. CMRO2 is calculated according to Fick's principle, incorporating multiple parameter maps for several aspects of the hemodynamic response into a measure of oxygen metabolism (Figure 1C and Methods). Figure 1C illustrates brain slices of non-thresholded parameter maps, averaged across all participants, alongside boxplots with each subject's average gray matter (GM) values in each condition. Table 1 provides the mean values of the individual parameters and CMRO2 across all subjects and conditions.

Table 1

Whole-brain (GM) parameter values, mean ± SD across subjects and conditions.

R2' [1/s]	CBV [%vol]	OEF [ratio]	CBF [ml/100g/min]	CMRO2 [µmol/100g/min]
5.3 ± 0.4	4.8 ± 0.2	0.39 ± 0.04	44.5 ± 7.2	127.8 ± 18.4

The BOLD signal is a composite signal representing the combined neurovascular and metabolic response lacking the ability to distinguish individual factors. The canonical hemodynamic response model that is commonly employed to interpret ΔBOLD (Figure 1D) assumes several stable relationships between hemodynamic parameters that might not be identical for each voxel. The most prominent assumption regarding the response to neuronal activity is that CBF provides excess oxygen to a stimulated region, surpassing the increased metabolic demands. The relationship between CBF and CMRO2 changes is described by the *n*-ratio, which commonly adopts values between 2-4, ultimately resulting in a task-induced positive BOLD response relative to an experimental baseline (ΔBOLD [%]). In this study, we combined BOLD and quantitative fMRI to quantify CBF and CMRO2 changes on a voxel level in response to different task conditions.

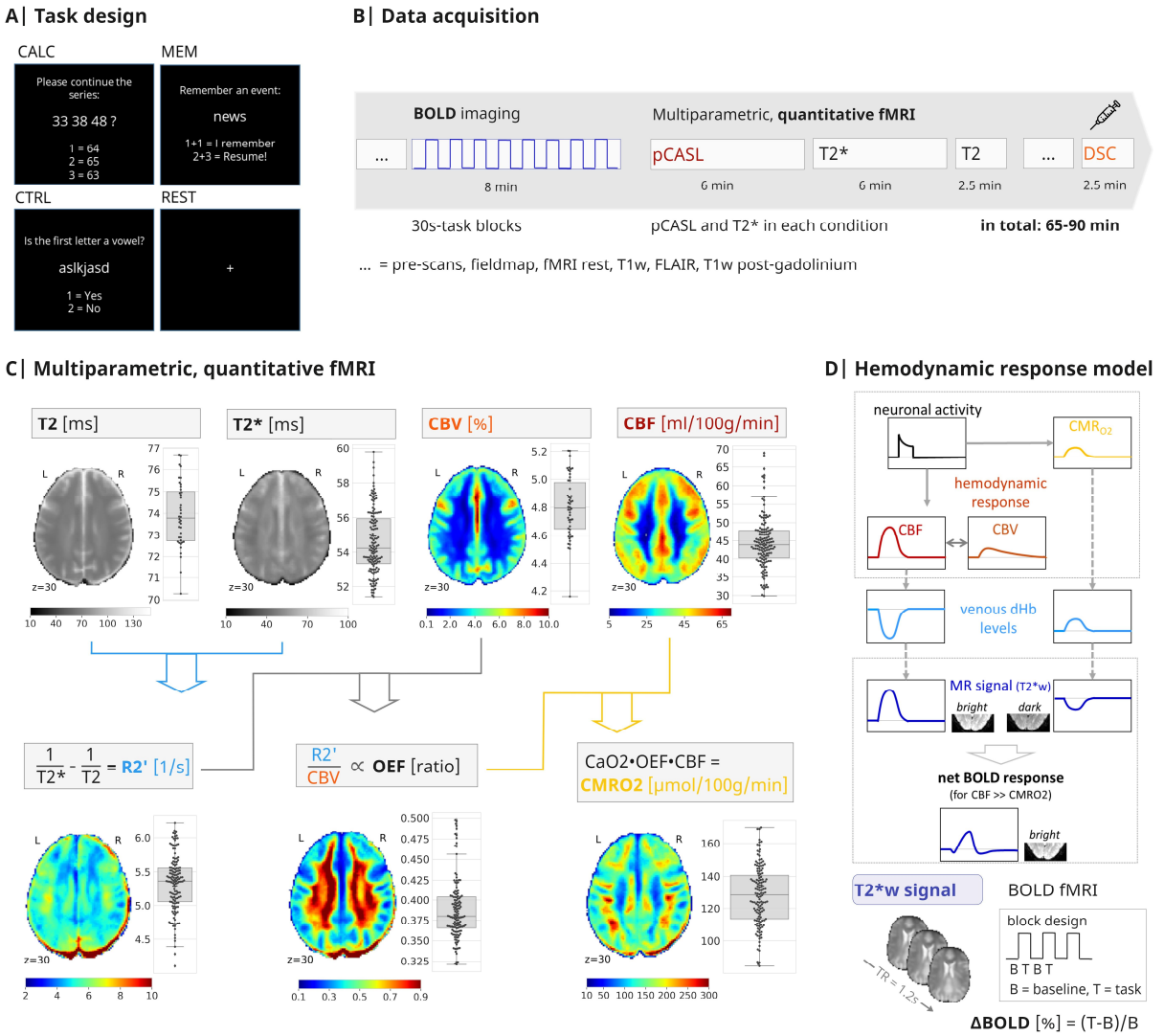

Figure 1. Study design, quantitative fMRI, and the hemodynamic response model of BOLD fMRI. A| We performed BOLD- and quantitative fMRI on healthy subjects performing four different conditions within the same imaging session: calculation task (CALC), autobiographical memory task (MEM), active control baseline (CTRL), and uncontrolled resting-state baseline (REST). **B|** During each imaging session, we acquired BOLD fMRI data with a 30-sec block design, together with multiparametric, quantitative BOLD (mqBOLD) data while conditions were presented in pseudo-randomized order: T2* mapping to measure both reversible and irreversible dephasing; pseudo-continuous arterial spin labeling (pCASL) to measure CBF during each condition; T2 mapping to once measure irreversible dephasing due to tissue properties; dynamic susceptibility contrast (DSC) MRI using a contrast agent to measure CBV during CTRL, at the end of the session. **C|** Quantitative fMRI delivers voxelwise CMRO2 by integrating T2, T2*, CBV, and CBF parameters via Fick's principle (see Methods section for detailed equations). Brain slices of subject-average parameter maps and boxplots illustrating average GM values (line, median; box limits, upper and lower quartiles; individual dots, subject average per condition). The reversible transverse relaxation rate (R2') reflects a voxel's overall deoxyhemoglobin (dHb) content. The OEF is proportional to R2'/CBV. Voxel-wise CMRO2 is then calculated as the product of OEF, CBF, and the arterial oxygen content of the blood (CaO2) as derived from individual measures of oxygen saturation and hematocrit. **D|** The canonical hemodynamic response model of the BOLD signal:

Increased neuronal activity leads to higher oxygen metabolism (CMRO2), decreasing oxygenation levels and increased dHb content in venous blood. Simultaneously, neurovascular coupling mechanisms cause an increase in CBV and CBF. This hemodynamic response counteracts the effects of oxygen metabolism, leading to a total decrease in dHb content. In BOLD-fMRI, the net fluctuation of dHb levels is dynamically measured with T2*-weighted (T2*w) echo planar imaging (EPI). ΔBOLD during any task condition is calculated by subtracting task (T) from baseline (B) T2*w data. Based on a canonical hemodynamic response function, positive BOLD signal changes are commonly interpreted as increased neuronal activity.

Negative BOLD signal responses do not necessarily indicate reduced oxygen metabolism

We conducted separate partial least squares (PLS) analyses on BOLD- and mqBOLD parameter maps to obtain statistically comparable results for BOLD and quantitative fMRI. These analyses yield bootstrap ratios (BSR), interpreted similarly to z-values (see Methods). Fig. 2A illustrates the cortical distribution of these statistical maps for the CALC vs. CTRL contrast, calculated in standard (MNI) brain space (see Fig. S1 for contrasts CALC vs. REST, and MEM vs. CTRL). We identified a widespread pattern of significant positive and negative ΔBOLD for the contrast CALC vs. CTRL. The histograms in Fig.2B illustrate the group-average, task-related changes for each parameter within masks of significant ΔBOLD (group BOLD masks: CALC-positive, CALC-negative).

ΔCBF and ΔCMRO2 within the CALC-positive mask showed amplitudes typical for a canonical positive response: ΔBOLD[%] = 0.37%, ΔCBF[%] = 6.6%, ΔCMRO2[%] = 3.1%, *n*-ratio (ΔCBF[%] / ΔCMRO2[%]) = 2.1 (Fig. 2B). Within the CALC-negative mask, however, absolute changes for ΔCBF and ΔCMRO2 were much lower in amplitude with values around zero, despite negative ΔBOLD being around 70% of the positive ΔBOLD amplitude (-0.26%). To avoid the influence of image distortions that might occur during the normalization of individual subject data to MNI group space, we also analyzed data in native space using individual BOLD masks. This analysis revealed significant positive ΔCBF and ΔCMRO2 with overall higher signal amplitudes within the CALC-positive mask, but no significant hemodynamic response within CALC-negative masks (Fig. 2C). We also investigated the spatial patterns and amplitudes of CALC compared to the REST baseline (Fig. S1A), where we observed a stronger ΔBOLD in both directions than compared to CTRL (Fig. S1B and C). Again, ΔCBF and ΔCMRO2 significantly increased in CALC-positive masks but were not significantly different from zero in CALC-negative masks across subjects ($p > .001$) (Fig. S1C). Finally, we replaced our PLS analysis of BOLD fMRI data with a second-level GLM model (see Fig. S4A and B) confirming that the median ΔCBF and ΔCMRO2 values within the CALC-negative regions were around zero (PLS/GLM-result CALC vs. CTRL contrast: ΔCBF = -0.83% / -0.71%; ΔCMRO2 = 0.43% / -0.02%).

Overall, parameter values for positive ΔBOLD were in line with a canonical hemodynamic response, with ΔCBF (in %) being at least ten times higher than ΔBOLD and more than twice

the amplitude of ΔCMRO2 (*n*-ratio of >2). However, we found no significant negative ΔCBF, ΔCBV, ΔT2* or ΔCMRO2 in the negative ΔBOLD masks across subjects.

We subsequently analyzed metabolic parameters on a regional level to control for the effect of averaging across various functional regions in brain-wide masks. We identified eight clusters with positive ΔBOLD and nine with negative ΔBOLD (Fig. 2D, left). Within those clusters, the median ΔCMRO2 is significantly positive in four out of eight positive BOLD clusters but negative in none of the negative BOLD clusters (Fig. 2D, bar plots). The two clusters with negative ΔBOLD in the auditory network (SMN 1, SMN 2) even exhibit a significant positive ΔCMRO2. Within circumscribed regions, we thus identified an average discordant ΔBOLD in 50% of positive BOLD clusters and in 100% of negative BOLD clusters.

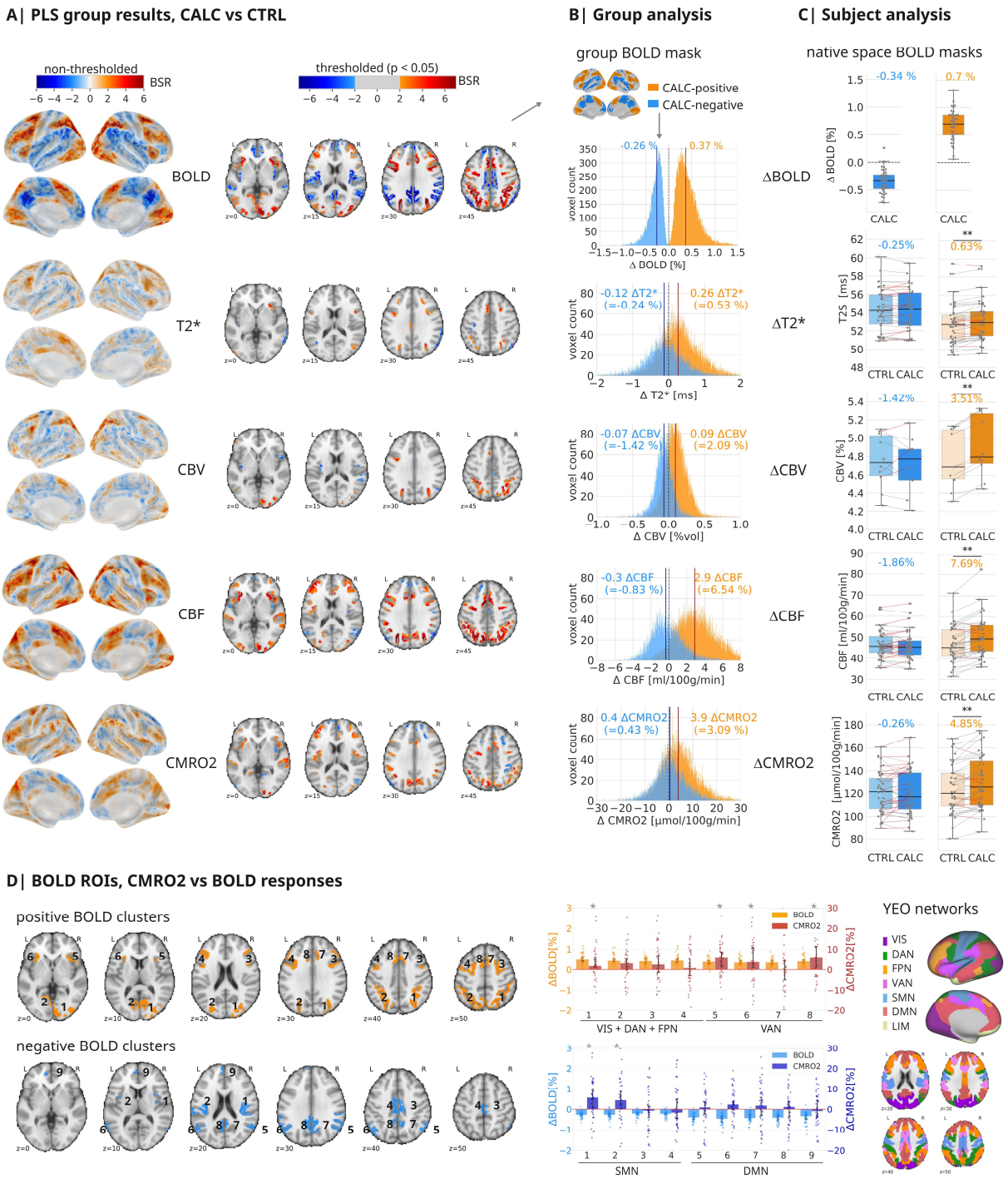

Figure 2. Negative BOLD signal changes do not indicate a reduction in oxygen metabolism. A| Statistical results of the PLS group analysis in standard MNI space, comparing CALC and CTRL, for both BOLD and quantitative fMRI parameter maps. Maps projected on the brain surface show non-thresholded bootstrap ratios (BSR, akin to z-values) of the first latent variable, which was significant in each analysis, i.e., for BOLD, CBF, CBV (N=10), T2* and CMRO2 respectively (permutation tests, $p < .001$). Red voxels indicate higher values during CALC than during CTRL, while blue voxels represent the opposite contrast. Axial slices display significant brain clusters, thresholded at BSR ±2 (akin to $p < .05$, cluster size > 30 voxels) for the BOLD, CBF, CBV, T2* and CMRO2 signals. **B|** Histograms depict group-average median voxel distributions of all parameters (CALC minus CTRL) within the binarized CALC-positive and CALC-negative group masks (shown as surface plot). **C|** Subject distribution of all

parameters in native space. Dots represent individual subject values, calculated as the median across voxels within individual BOLD masks of significant positive (orange) and negative (blue) ΔBOLD. Paired samples, two-sided t-tests, ** $p < .001$. Gray lines connect values obtained from individual subjects, and red lines indicate subjects where the sign of ΔCBF or ΔCMRO2 deviates from the BOLD-indicated direction. **D|** Regional clusters (designated by numbers) of positive and negative ΔBOLD (PLS group results, thresholded at BSR > ±3) and associated bar plots showing ΔBOLD and ΔCMRO2. Please note the different axes for ΔBOLD versus ΔCMRO2. Bars indicate ΔBOLD[%] and ΔCMRO2[%] median across voxels, error bars 95% CI, 2000 bootstraps, and dots represent subject values. Any signal increase or decrease where error bars cross the zero line is considered non-significant; an asterisk denotes $p < 0.05$. Clusters are located in different functional networks, as depicted on the brain surface and in axial slices (Thomas Yeo et al., 2011): visual (VIS); dorsal attention (DAN); frontoparietal (FPN); ventral attention (VAN); somatomotor (SMN); default mode (DMN) network.

There could be several reasons for the absence of hemodynamic and metabolic changes, particularly related to negative ΔBOLD: i) voxel-specific characteristics or confounds of the MRI signal, ii) lower sensitivity of the imaging methods to detect negative ΔCBF or ΔCMRO2 of smaller amplitudes, or iii) different hemodynamic mechanisms in specific voxels or regions. In the following, we will explore each of these potential explanations.

First, we analyzed ΔBOLD and ΔCMRO2 for the other contrasts, MEM vs. REST (Fig. S1A-D) and MEM vs. CTRL (Fig. S1D-G). Across voxels of the CALC-positive and CALC-negative masks, we found overall larger ΔBOLD, ΔT2*, ΔCBF, and ΔCMRO2 compared to the CTRL baseline, yet the changes within the CALC-negative masks were still not significant across subjects (Fig. S1D). Across all voxels of the MEM-positive and MEM-negative masks (Fig. S1E) and also on the subject level (Fig. S1G), we found similar BOLD signal amplitudes as for the CALC condition, again with stronger positive than negative ΔBOLD. When analyzing the quantitative data, we observed significant positive ΔCBF and ΔCMRO2 in the MEM-positive mask but no significant changes in the MEM-negative mask. This suggests that, on average, and across different task conditions, positive ΔBOLD indicates significant positive ΔCMRO2, but the metabolic interpretation of negative ΔBOLD is less clear.

Most voxels with positive ΔBOLD during MEM were found within the default mode network (DMN), where we had already identified negative ΔBOLD during CALC (Fig. S1F). As a control analysis for voxel-specific characteristics that might alter the sensitivity to detect hemodynamic responses, the overlap between MEM-positive and CALC-negative masks allowed us to study CBF and CMRO2 responses for positive and negative ΔBOLD within the same voxels. Fig. S1H shows the histograms of ΔBOLD, ΔCBF, and ΔCMRO2 for all voxels of a conjunction mask (MEM-positive ∧ CALC-negative). On average, we found a canonical hemodynamic response for positive ΔBOLD (0.32%) caused by a substantial increase in ΔCBF (5.94%) and a positive ΔCMRO2 (3.54%). However, for negative ΔBOLD (-0.29%), the ΔCBF (-0.47%) was much weaker than expected within the canonical framework, i.e., for a negative

response of similar magnitude to the positive response within the same voxels. Thus, the low ΔCBF together with a positive ΔCMRO2 results in a negative ΔBOLD.

A summary of subject-average changes for all parameters and all task contrasts is presented in Table 2. Altogether, we found a consistent relationship for positive ΔBOLD-ΔCMRO2, yet with regional variability (Fig. 2D). Crucially, the discrepant results for positive and negative ΔBOLD within 'conjunction voxels' (Fig. S1H) indicate that the absence of a canonical hemodynamic response for negative ΔBOLD cannot be explained by voxel characteristics such as vascular composition or reactivity, as the same voxels show a canonical hemodynamic response for positive ΔBOLD.

Table 2

Mean BOLD signal change and relevant parameter values of the mqBOLD approach across subjects (standard deviation) within individual BOLD-fMRI masks, separately for positive and negative BOLD responses.

task baseline	**BOLD mask**	**BOLD** [%]	**CBF** [ml/100g/min]		**CMRO2** [µmol/100g/min]		**OEF** [ratio]	
			baseline	ΔCBF	baseline	ΔCMRO2	baseline	ΔOEF
CALC CTRL	CALC-pos	**0.70%**	46.5 (8.2)	**7.7%** 3.1** (3.2)	124.0 (20.9)	**4.9%** 6.4** (7.7)	0.37 (0.06)	**-3.2%** -0.013** (0.01)
	CALC-neg	**-0.34%**	46.6 (6.4)	-1.9% n.s.	120.1(18.1)	-0.3% n.s.	0.35 (0.05)	0.01% n.s.
MEM CTRL	MEM-pos	**0.51%**	48.5 (9.1)	**5.6%** 2.6** (2.8)	125.0 (18.8)	**5.1%** 6.4** (8.2)	0.36 (0.06)	**-0.7%** -0.003* (0.013)
	MEM-neg	**-0.35%**	48.4 (8.9)	-1.7% n.s.	126.7 (31.1)	-1.1% n.s.	0.36 (0.07)	1.1% n.s.
CALC REST	CALC-pos	**1.01%**	45.3 (8.8)	**10.0%** 4.4** (3.2)	123.5 (24.5)	**6.4%** 6.5** (8.1)	0.38 (0.06)	**-3.6%** -0.014** (-0.014)
	CALC-neg	**-0.38%**	47.7 (7.8)	-2.6% -1.2 (3.6)	123.7 (20.3)	-0.9% n.s.	0.36 (0.06)	1.0% n.s.

Note. Quantitative values (black font) of CBF, CMRO2, and OEF are displayed both at baseline and as absolute delta values (task minus baseline), along with percent change values (colored) for each contrast. Values reflect data as displayed in Fig. 2C, with CMRO2 values in CALC being corrected for CBV increases, see Methods. ** $p < .001$, based on paired, two-sided t-tests, $df = 39$ for CALC vs. CTRL contrasts, $df = 29$ for CALC vs. REST and MEM vs. CTRL contrasts.

Control analyses

According to the hemodynamic response model (Fig. 1D), changes in CBF are the main contributor to the neurovascular coupling mechanism. Therefore, we performed several control analyses to validate the sensitivity of pCASL imaging to detect ΔCBF (Fig. S2).

We identified magnitudes of ΔCBF ranging from -12% to +29%, and regions with positive ΔCBF exhibited a higher *n*-ratio than regions with negative ΔCBF (Fig. S2A). Moreover, our pattern of negative ΔCBF during CALC corresponds to the localization of negative ΔCBF observed with PET (Fig. S2B). Please note that Fig. S2 shows the CALC vs. REST contrast, as classical DMN literature usually relies on task contrasts to a REST baseline. Notably, areas showing significant CBF decreases from PET and MRI data are spatially less widespread than those with BOLD signal decreases (Fig. S2B, group PLS results) and predominantly centered around peak regions, as shown in Fig. S2A. Additionally, the homogeneity of OEF across GM is similar to that derived from PET imaging (Fig. S2C).

Subsequently, we evaluated the stability of BOLD and CBF signals across continuous task performance. In the main study (Fig. 1), block durations vary for BOLD (30 sec) and quantitative (approx. 6 min) fMRI to achieve the best signal-to-noise ratio (SNR) for each modality. To investigate signal stability across more extended periods of task performance, we collected BOLD fMRI data in a separate control study (N=18) while participants continuously performed the CALC and MEM tasks during 3-minute task blocks. Fig. S2D demonstrates that the BOLD signal remains constant throughout task performance, suggesting no evidence for habituation or drift effects. Additionally, the average amplitudes of ΔBOLD in the control study were similar to those observed in our main study (ΔBOLD[%] CALC-positive/CALC-negative/MEM-positive: 0.6%/-0.46%/0.34%; main study: 0.70%/-0.34%/0.51%). Finally, the time-resolved analysis of pCASL-data from the main study shows that CBF remained constant throughout the entire measurement blocks (Fig. S2E).

Empirical validation of the Davis model explaining concordant and discordant BOLD signal responses

In the following section, we evaluate the consistency of discordant ΔBOLD-ΔCMRO2 relationships on the voxel level and compare our empirical data to an established model of hemodynamic responses. The Davis model (Davis et al., 1998) predicts the extent of BOLD responses for a realistic range of ΔCMRO2[%] and ΔCBF[%] across the cortex. Fig. 3A displays the model's prediction of ΔBOLD (contours, -3% to +3%) for a set of typical hemodynamic response parameters. The model illustrates that a canonical BOLD signal response emerges when ΔCBF exceeds ΔCMRO2, with ΔBOLD, ΔCBF, and ΔCMRO2 all changing in the same direction. In other terms, a positive ΔBOLD emerges for a *n*-ratio > 1. However, the model also indicates that ΔBOLD may conflict with the actual metabolic changes if ΔCBF is lower than ΔCMRO2 (i.e., for an *n*-ratio <1) or if ΔCBF and ΔCMRO2 have opposite signs. These areas of discordance between ΔBOLD and ΔCMRO2 are highlighted by violet shadings in Fig. 3A. For instance, a negative ΔBOLD of -1.3% would be measured if CBF increases by only about 5% during a ΔCMRO2 of +23%. In other words, an identical metabolic change can result in opposite signs of the BOLD signal, depending on the extent of ΔCBF. Since we have measured ΔBOLD, ΔCBF and ΔCBV and subsequently calculated ΔCMRO2, our data are well-suited to assess the

consistency of the Davis model with empirical data. Importantly, in Fig. 3, we calculate voxel CMRO2 from our OEF and CBF imaging data using Fick's principle and then compare it to predictions from the Davis model.

Fig. 3B shows subject-average data of ΔCBF versus ΔCMRO2 for CALC vs. CTRL, with colors indicating positive or negative ΔBOLD, across all GM voxels of the cortex (see also Fig. S3A for CALC vs. REST, and Fig. S3B for MEM vs. CTRL). To address issues with SNR when integrating all imaging modalities at the voxel level, we used less noisy ΔR2' derived from BOLD-fMRI for the CMRO2 calculation (see Methods and Fig. S5 for a sensitivity analysis). Our experimental data support several predictions of the Davis model. Overall, voxels exhibiting positive and negative ΔBOLD are located above and below a straight line with a slope of 1, indicating a *n*-ratio of >1. Importantly, these data also confirm the existence of a significant number of voxels with ΔBOLD opposite to their metabolic response, which we termed discordant responses. Such discordant responses are represented by red voxels on the left and blue voxels on the right side of zero ΔCMRO2 (Fig. 3B, red dashed line). Essentially, discordant voxels exhibit positive ΔBOLD despite negative ΔCMRO2 and vice versa. Importantly, if we were to interpret the activity in those voxels based solely on BOLD fMRI data and assuming a canonical hemodynamic response across the entire cortex, the activity in those voxels would be misinterpreted.

To provide a more precise illustration of the location of discordant voxels, we split the data from Fig. 3B into two distinct scatter plots for CALC-positive (top) and CALC-negative (bottom) contrasts only (Fig. 3C). In both plots, voxels with discordant ΔBOLD compared to ΔCMRO2 were highlighted by violet shading. The total number of discordant voxels amounts to 31% and 66% for positive and negative ΔBOLD, respectively (Fig. 3C, pie charts). The second pie chart in the lower scatter plot demonstrates a similar ratio of discordant voxels when only including negative ΔBOLD voxels within the DMN, the network with the most consistently reported negative BOLD signal responses. Furthermore, the brain slices demonstrate that discordant voxels are spatially distributed across the cortex (Fig. 3C, spatial distribution). The stacked bar plots reveal that discordant voxels are equally distributed among voxels with the lowest to highest quartile of BOLD signal amplitudes (Fig. 3C, BOLD amplitude distribution, q1 represents the lowest quartile and q4 represents the highest quartile of BOLD signal amplitudes).

We also performed the same analyses for the CALC vs. REST (Fig. S3A) and MEM vs. CTRL (Fig. S3B) contrasts. We likewise observed the presence of discordant voxels across the entire range of ΔBOLD. Specifically, discordant voxels accounted for 36%/52% of significant positive/negative ΔBOLD voxels in the CALC vs. REST contrast and for 12%/54% in the MEM vs. CTRL contrast. Again, discordant voxels were distributed throughout the entire cortex.

Fig. 3D summarizes the distribution of subject-median parameter values across concordant and discordant voxels. ΔBOLD in concordant voxels (Fig. 3D, yellow/turquoise bars) is consistent with a canonical hemodynamic response with a median *n*-ratio (ΔCBF/ΔCMRO2 per voxel) of 2.0 and 1.6 across concordant positive and negative ΔBOLD, respectively. However, a

considerable number of discordant voxels (Fig. 3D, violet bars) show ΔBOLD opposite to their metabolic response and a lower ΔCBF than expected by the canonical model. Importantly, discordant ΔBOLD occurs in one-third of voxels with positive ΔBOLD and in two-thirds of voxels with negative ΔBOLD and across different task conditions. Moreover, discordant voxels are uniformly dispersed throughout the cortex and arise within all ranges of ΔBOLD magnitudes.

The discordance between ΔBOLD and ΔCMRO2 might emerge from partial volume effects when integrating voxel data from imaging sequences with heterogeneous voxel sizes, as occurring in our main study. We thus performed a replication study (N=10) using the identical task design (CALC vs. CTRL) and analysis pipeline of the main study yet acquired data with adjusted MRI sequences to achieve harmonized voxel matrices across all parameter maps of BOLD and mqBOLD data (see Methods section). The results of the replication study were consistent with those of the main study (Fig. S6). We found that 40% of all voxels with either significant positive or negative ΔBOLD were classified as discordant. As in the main study, discordant voxels showed smaller CBF responses than expected from a canonical neurovascular coupling.

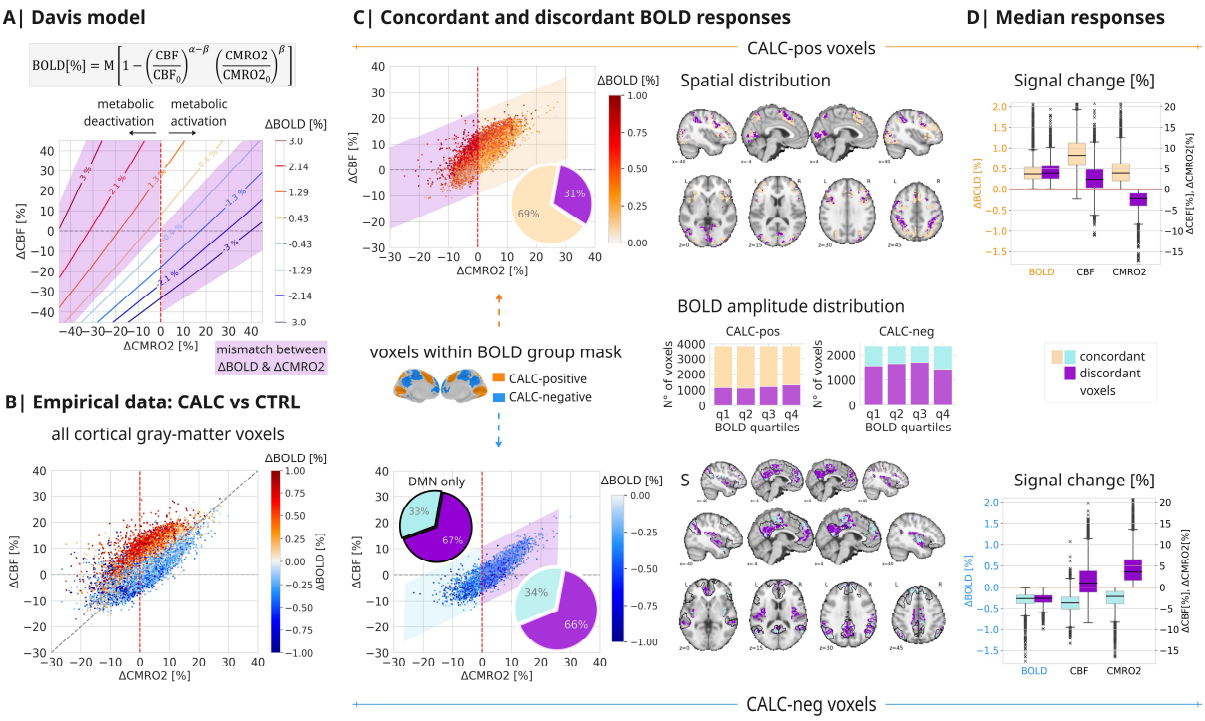

Figure 3. Dependence of BOLD responses on changes in CBF and CMRO2. A| Visualization of the Davis model. Predicted BOLD responses (ΔBOLD[%]) are depicted as colored contour lines across ΔCBF[%] and ΔCMRO2[%]. The model illustrates that, for a given ΔCMRO2[%], the sign and amplitude of the BOLD response depend on the amplitudes of ΔCBF[%]. The canonical hemodynamic response assumes that ΔCBF surpasses ΔCMRO2, resulting in a positive ΔBOLD and vice versa for negative BOLD signal changes. However, the Davis model also predicts a range of BOLD responses with discordant signs compared to the change in underlying metabolic activity (violet shading). **B|** Empirical data from BOLD- and quantitative fMRI for all cortical voxels. ΔCMRO2 was calculated from BOLD-derived ΔR2' (see

Methods), median across all subjects per voxel, with colors indicating ∆BOLD[%]. Our experimental data replicate the slope and range of values as predicted by the Davis model, particularly demonstrating a substantial number of voxels with ∆BOLD opposing ∆CMRO2. **C|** Voxels with significantly positive (top) and negative (bottom) BOLD responses from (B) are plotted separately here. Voxels with ∆BOLD concordant to ∆CMRO2 are depicted on a pale (yellow/turquoise) background, while voxels with discordant ∆BOLD are shown on a violet background. The pie plots summarize the ratio of discordant to concordant voxels. In the lower panel, the pie plot with black contours summarizes the ratio of discordant voxels within only the DMN. Axial slices illustrate the spatial distribution of significantly concordant and discordant BOLD voxels, with black contours indicating the DMN. The stacked bars in the right center depict the amplitude distribution of discordant and concordant voxels across BOLD amplitude quartiles. It is noteworthy that discordant voxels show neither spatial nor amplitude preference. **D|** The boxplots summarize ∆CMRO2[%] and ∆CBF[%] across all voxels with either concordant or discordant ∆BOLD[%]; line, median; box limits, upper and lower quartiles. Please note that discordant and concordant voxels feature a similar ∆BOLD amplitude distribution despite indicating opposite metabolic responses.

In a final step, we directly estimated the parameters used in the Davis model from our own data. Since we acquired data on ΔBOLD, CBV, OEF, and CBF, we were able to directly estimate the values of α and the subject-specific calibration factor M from our empirical data. We found an average α of 0.38 and an M of 11.2 ± 1 % (N = 40 subjects). Fig. S8 replicates Fig. 3, where CMRO2 was quantified using the Davis model instead of Fick's formula.

Consistency of concordant or discordant BOLD signal responses depends on baseline OEF

In the following section, we used the conjunction mask from the CBF control analysis above (voxels with both positive and negative BOLD responses during either CALC or MEM) to investigate whether these identical voxels show a consistent hemodynamic response pattern for both negative and positive ΔBOLD. We categorized each voxel based on whether it either showed consistent concordant ('concordant only') or discordant ('discordant only') ΔBOLD in both tasks or if it displayed a mixed response ('mixed' voxels), i.e., a concordant BOLD signal response in one condition but a discordant one in the other task (Fig. 4A). The pie chart displays that the majority of voxels (48%) showed a mixed response. In contrast, 18% and 35% consistently showed a discordant and concordant response, respectively. Fig. 4B shows the spatial and amplitude distributions of ΔCBF and ΔCMRO2 in relation to ΔBOLD for each of the three voxel types. The 'concordant only' voxels show a canonical hemodynamic response with an *n*-ratio of around two, independent of the task condition or the sign of the BOLD signal response (Fig. 4B, yellow/turquoise bars). In contrast, 'discordant only' voxels lack a canonical hemodynamic response for either direction of ΔBOLD (Fig. 4B, violet/lilac). The 'mixed' voxels (Fig. 4B, red/orange) show a canonical hemodynamic response with a surplus of ΔCBF for positive ΔBOLD but lack a significant ΔCBF for negative ΔBOLD.

As changes in CMRO2 without an adequate CBF response can only be accommodated via changes in OEF, we tested whether the three types of voxels differ in their OEF during baseline states. We speculated that 'discordant only' voxels, with the lowest ΔCBF during a task, would have the lowest baseline OEF (indicating the highest oxygen buffer). In line with this hypothesis, we found that baseline OEF was gradually lower from 'concordant only' through 'mixed' to 'discordant only' voxels (Fig. 4C). Together, this suggests that 'discordant only' voxels have a sufficient oxygen buffer to accommodate changes in oxygen demand via ΔOEF. In contrast, voxels with a high baseline OEF need to regulate additional oxygen demand via CBF. Please note that OEF was acquired independently from CBF data using the mqBOLD approach.

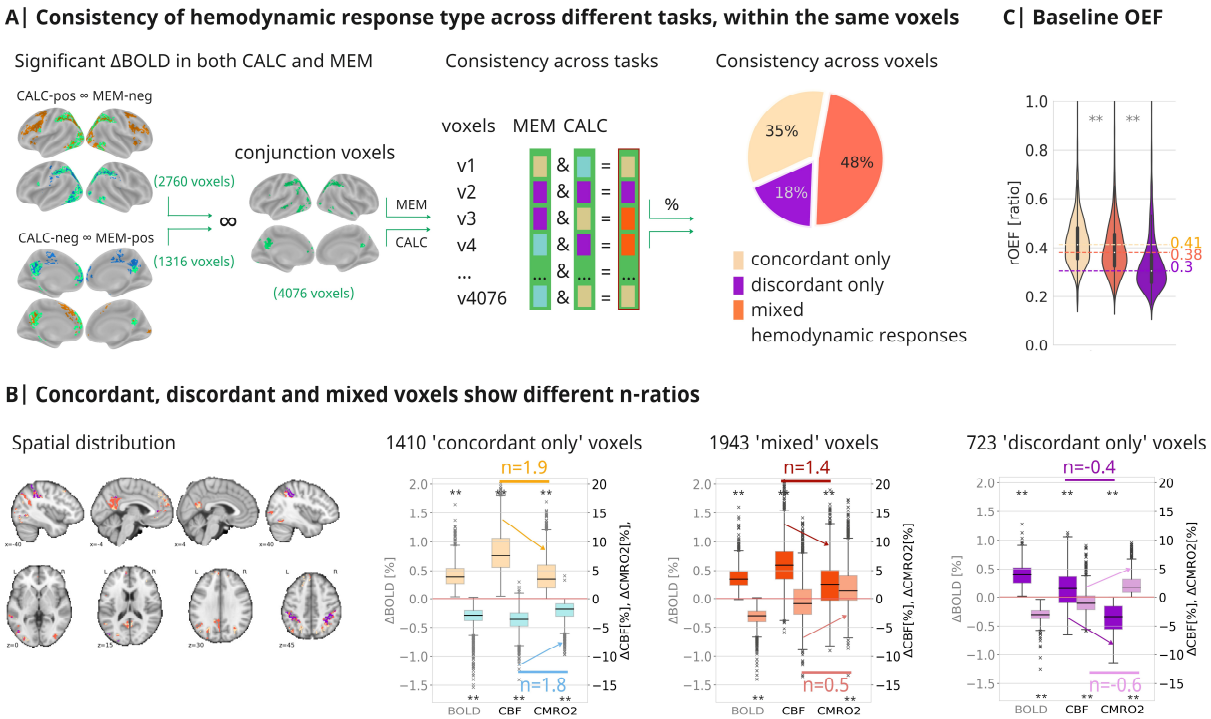

Figure 4. Concordant or discordant BOLD signal responses depend on baseline OEF. A| Conjunction voxels (green outlines) – showing positive and negative BOLD signal changes during either CALC or MEM – were sorted according to their response type. The pie chart summarizes the consistency of response types across voxels: 35% of all conjunction voxels showed concordant responses (same sign of ΔBOLD and ΔCMRO2) during both MEM and CALC conditions ('concordant only'). 18% of all conjunction voxels showed discordant responses in both conditions ('discordant only'). 48% of the conjunction voxels ('mixed' voxels) showed concordant responses in one condition but discordant responses in the other. **B|** Spatial distribution is depicted on brain slices using consistent color overlays: 'Concordant only' and 'mixed' voxels mainly cluster in regions of the DMN, while 'discordant only' voxels occur in the medial part of the VAN. The boxplots illustrate subject-median parameter values separately for 'concordant only,' 'mixed,' and 'discordant only' voxels. While the range of ΔBOLD is similar across the three groups, ΔCBF and ΔCMRO2 vary strongly as expressed by their *n*-ratios. Asterisks indicate significant differences from zero, tested via independent t-tests corrected for multiple comparisons. **C|** The three voxel groups exhibit significantly different OEF during CTRL baseline, with 'concordant only' voxels having significantly higher OEF and 'discordant only' voxels having significantly

lower OEF than 'mixed' voxels. ** $p < 0.001$, independent sample permutation test on the median values, conducted for 'mixed' versus the two other voxel types, 2000 permutations.

Baseline OEF relates to different hemodynamic response types

We then investigated the baseline hemodynamics across the entire cortex. We pooled all voxels with significant ΔBOLD during either task (CALC, MEM), which accounted for 53% of all GM voxels, and grouped them into voxels of concordant ΔBOLD, discordant ΔBOLD, and voxels not involved in any task (Fig. 5A, pie chart). We then analyzed the relationship between baseline CMRO2 and CBF, OEF, and CBV and found a significant linear correlation between CMRO2 and all three hemodynamic parameters, consistent across all voxels (Fig. 5A) and in line with our calculations based on Fick's principle.

Next, we used multiple linear regression analysis to assess the individual contribution of baseline OEF, CBF, or CBV to the variance of baseline CMRO2 across concordant and discordant voxels. The model was significant, with similar model parameters for each group (concordant model: $F(3,21809) = 72070$, $p < .001$, CMRO2 = 139.9 + 321.1*OEF + 3.3*CBF + 0.4*CBV + e, R^2=0.91; discordant model: $F(3,14544) = 48390$, $p < .001$, CMRO2 = 128.1 + 309.2*OEF + 3.2*CBF + 1.3*CBV + e; R^2=0.91; all predictors mean-centered, p<.001 for all beta values). In summary, baseline OEF consistently accounts for >68% of CMRO2 variability across concordant and discordant voxels, followed by CBF (>28%) and CBV (>1%). Notably, discordant voxels also have a lower baseline metabolism than concordant voxels, as indicated by the parameter values of CMRO2. We then assessed whether concordant and discordant voxels differ in their average baseline levels of CBF, OEF, and CBV. Across subjects, concordant voxels show significantly higher CBF, higher OEF, and lower CBV than discordant voxels during baseline (Fig. 5B).

To independently support our finding of lower OEF and higher CBV in discordant voxels, we used two external quantitative susceptibility mapping (QSM) datasets of the human brain (Fig. 5C). We projected our masks of concordant and discordant voxels onto these high-resolution data and tested for differences between the two groups of voxels. We observed similar susceptibility values among concordant and discordant voxels, yet a slightly but significantly lower median for discordant voxels (Fig. 5C, top) in the first dataset (Huck et al., 2019). This indicates a lower dHB content and aligns with the lower OEF we observed in our data. Moreover, we found a significantly higher venous density for discordant voxels (Fig. 5C, bottom) in the second dataset (Lüsebrink et al., 2021), which is also in line with the higher CBV values we observed in our data.

In the final step, we asked whether ΔOEF might serve as an alternative mechanism to ΔCBF in accommodating oxygen demand during task processing. We used multiple linear regression to assess the individual contributions of ΔCBF and ΔOEF to the variance of ΔCMRO2 across all task conditions. We identified two distinct patterns of hemodynamic responses for concordant and discordant voxels (Fig. 5D). In concordant voxels, ΔCMRO2 is primarily modulated by ΔCBF:

F(2,21971) = 67980, $p < .001$, with ΔCBF explaining 87% and ΔOEF 16% of a total explained variance of R^2=0.86 of the model (ΔCMRO2[%] = 2.6 + 0.83*ΔOEF[%] + 0.86*ΔCBF[%] + e; all predictors mean-centered, p<.001 for all beta values). In contrast, discordant voxels exhibit a different hemodynamic response, where ΔCMRO2 is primarily modulated by ΔOEF: F(2,14694) = 39320, $p < .001$, with ΔOEF explaining 58% and ΔCBF 42% of a total explained variance of R^2=0.84 of the model (ΔCMRO2[%] = 1.2 + 1.1*ΔOEF[%] + 0.88*ΔCBF[%] + e; all predictors mean-centered, p<.001 for all beta values). In summary, concordant voxels regulate ΔCMRO2 primarily via ΔCBF (87%), while discordant voxels predominantly regulate their oxygen demand via ΔOEF (58%) and only secondary via ΔCBF (42%). As we obtained empirical ΔCBV only for the CALC-CTRL contrast, we could not include it in these regression models. Furthermore, it should be noted that the negative correlation between ΔCMRO2 and ΔOEF for concordant voxels (Fig. 5D, middle plot) results from the compensatory rise in oxygenation levels during the surplus of ΔCBF.

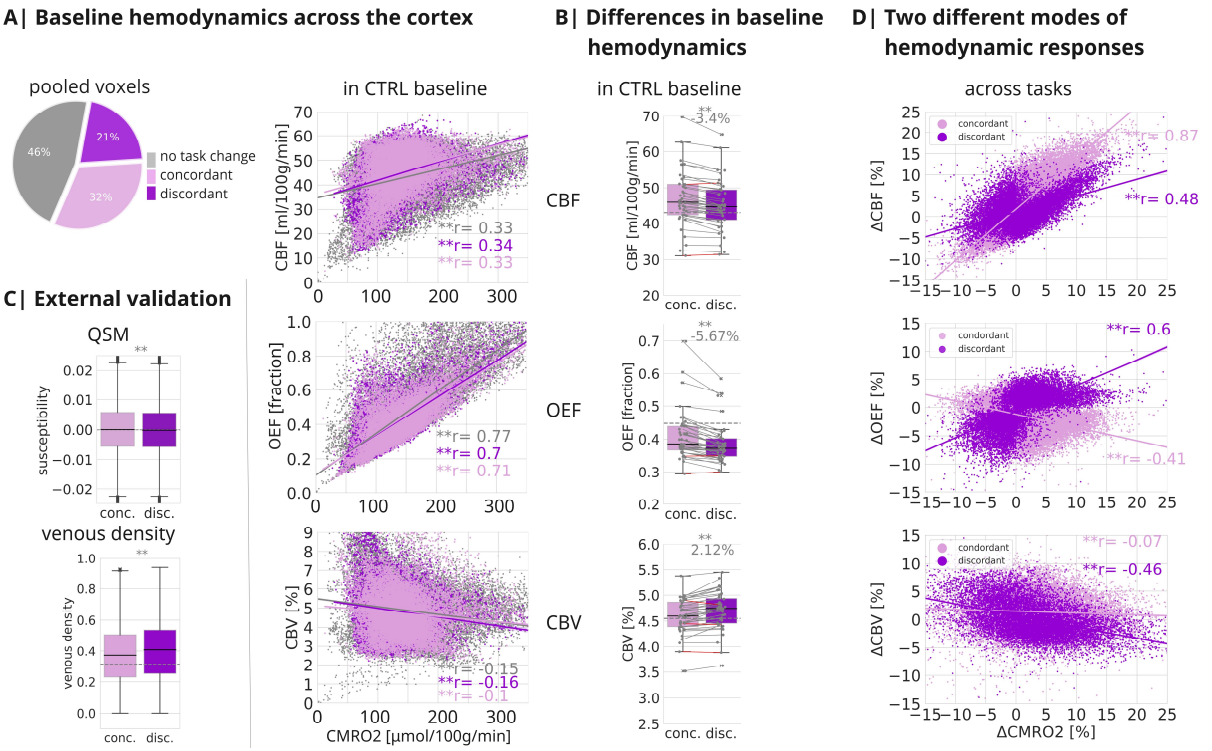

Figure 5. Two types of hemodynamic responses via changes in CBF or OEF. A| Across all task conditions, 21% of all GM voxels showed discordant, 32% showed concordant responses, and 46% were not significantly involved in any task. Regression plots: During baseline, CMRO2 and CBF show a medium correlation (Pearson's $r > 0.32$, $p < .001$), CMRO2 and OEF are highly correlated ($r > 0.7$, $p < .001$), and CMRO2 and CBV show a weak negative correlation ($r < -0.1$, $p < 0.001$) across all groups of voxels. **B|** Across subjects, discordant (disc.) voxels, on average, show significantly lower CBF (-3.4%), OEF (-5.7%), and higher CBV (2.1%) than concordant (conc.) voxels (paired-samples, two-sided t-test, $p < .001$). Boxplots: line, median; box limits, upper and lower quartiles; gray line, median of remaining GM voxels. **C|** Marginally, but significantly lower baseline susceptibility (QSM) and higher venous density in discordant vs. concordant voxels, revealed by two external datasets (Huck et al., 2019;

Lüsebrink et al., 2021). Boxplots: line, median; box limits, upper and lower quartiles; gray line, median of remaining GM voxels. ** $p < .001$, independent samples permutation test on the median values, conducted for discordant versus concordant voxels, 2000 permutations. **D|** Correlation of ΔCMRO2[%] with either ΔCBF[%], ΔOEF[%], or ΔCBV[%] across all task contrasts (CALC or MEM vs. CTRL), separately for concordant (pale) and discordant (dark violet) voxels. ΔCMRO2 and ΔCBF showed a strong positive correlation across concordant voxels ($r = .87$, $p < 0.001$) and a moderate correlation across discordant voxels ($r = .48$, $p < .001$). In contrast, ΔCMRO2 and ΔOEF showed a moderate, positive correlation across discordant voxels ($r = .60$, $p < .001$) and a weak, negative correlation across concordant voxels ($r = -.41$, $p < .001$). ΔCBV could only be evaluated for a subset of 10 subjects and only across the CALC vs. CTRL contrast, see Methods. ΔCMRO2 and ΔCBV across this subset showed a weak correlation around zero across concordant voxels ($r = -.07$) and a moderate, negative correlation across discordant voxels ($r = -.46$, $p < 0.001$).

DISCUSSION

In this study, we examined the consistency between BOLD signal responses and changes in oxygen metabolism across gray-matter voxels throughout the human cortex. Such a finding would provide crucial evidence for the common interpretation of positive and negative ΔBOLD as indicators of increased or decreased neuronal activity. In contradiction to the canonical BOLD response model, our results show that around 40% of brain voxels with significant BOLD signal changes, measured during different task conditions, displayed opposite changes in oxygen metabolism. Specifically, discordant voxels with positive ΔBOLD showed a decrease in ΔCMRO2, while those with negative ΔBOLD exhibited an increase in ΔCMRO2. By measuring changes in BOLD signal, CBF, OEF, and CMRO2 within the same imaging session, we identified different neurovascular mechanisms for brain regions showing concordant and discordant responses. Discordant voxels regulate changes in oxygen demand primarily via ΔOEF, while only concordant voxels show a surplus of ΔCBF, as predicted by the canonical hemodynamic response. Additionally, we found lower baseline CMRO2 and OEF in discordant voxels, suggesting that their baseline oxygen supply is sufficient to meet changes in metabolic demand. In conclusion, we have identified two types of hemodynamic responses to changes in neuronal activity, which seem to depend on baseline OEF and metabolism.

Average BOLD and mqBOLD signals suggest a canonical hemodynamic response for positive ΔBOLD

In this study, we combined BOLD with mqBOLD fMRI to investigate hemodynamic and metabolic changes in relation to BOLD signal changes. Participants performed cognitive tasks eliciting both positive and negative BOLD signal responses across the cortex. Specifically, we aimed to elicit both response types within the same voxels, allowing us to directly compare their hemodynamic responses. To this end, we employed a cognitively demanding calculation task that induces positive ΔBOLD in somatosensory, frontoparietal, and ventral- and dorsal attention regions (Amalric & Dehaene, 2016; Fehr et al., 2007; Lin et al., 2011a) while simultaneously causing negative ΔBOLD in regions of the DMN (Anticevic et al., 2012; Raichle et al., 2001; Shulman, FIEZ, et al., 1997; Smallwood et al., 2021). Additionally, participants engaged in an autobiographical memory task known to induce positive ΔBOLD in regions of the DMN, partly overlapping with those of negative ΔBOLD during CALC (Andrews-Hanna et al., 2014; Davey et al., 2016; Ino et al., 2011; Spreng & Grady, 2010).

We also considered the issue of different baseline states in our study. The BOLD signal response to cognitive tasks is usually compared to low-level control tasks as baseline conditions (Addis et al., 2007; Burianova et al., 2010; Burianova & Grady, 2007a; DuPre et al., 2016; Spreng et al., 2010; Spreng & Grady, 2010). Studies showing negative ΔBOLD, however, typically compare against an experimentally uncontrolled resting state (Anticevic et al., 2012; Lin et al., 2011a; Pfefferbaum et al., 2011; Raichle et al., 2001; Singh & Fawcett, 2008). Hence, we included both types of baseline conditions in our study. All our task conditions elicited BOLD signal responses

as expected. Averaged across voxels, negative BOLD signal responses were about 50-70% of the amplitude of positive ΔBOLD (Fig. 2). Moreover, we found that ΔBOLD was larger when compared to REST than to CTRL baseline (Table 2, Fig. S1A-C).

Compared to BOLD fMRI, which requires subtraction analyses between conditions, the mqBOLD approach delivers quantitative measures for each condition. During CTRL baseline, we observed average GM values of CMRO2 and hemodynamic parameters (see Table 1) as previously reported for the healthy human brain (Aoe et al., 2018; Cho et al., 2018; Gauthier & Hoge, 2012; Ito et al., 2021; Lee & Wehrli, 2022; Leontiev & Buxton, 2007; Liang et al., 2013; Raichle et al., 2001; Stone & Blockley, 2017b; Wise et al., 2013; J. Zhang et al., 2015, 2015). Similarly, task-related changes (see Table 2) aligned with previous results (Gauthier et al., 2012; Restom et al., 2008; Y. Zhang et al., 2021). Analyzing mqBOLD data in relation to positive ΔBOLD, we found a concordant relationship between average BOLD signal changes and the quantitative parameters, fitting a canonical hemodynamic response (DiNuzzo et al., 2023; Uludağ et al., 2004), with ΔCMRO2 and ΔCBF surpassing ΔBOLD by factors of 10-20, resulting in a *n*-ratio of around 2 (Fig. 2).

Discordant hemodynamic responses for regions with positive ΔBOLD and overall for negative ΔBOLD

Despite evidence for a canonical hemodynamic response for the average of positive ΔBOLD, we did not find any significant hemodynamic or metabolic changes for the average of negative ΔBOLD across subjects (see CALC vs CTRL, Fig. 2C) for either task condition (see MEM vs CTRL, Fig. S1G) or when comparing against REST baseline (see Fig. S1C). Interestingly, we also observed significant deviations from the canonical response in clusters with positive ΔBOLD in a region-specific analysis. On average, we identified non-significant ΔCMRO2 in four out of eight clusters with positive ΔBOLD and in all nine clusters with negative ΔBOLD (Fig. 2D). One could argue that voxels with discordant ΔBOLD might suffer from voxel-specific artifacts such as partial volume effects or sparse vasculature, thereby lacking a significant ΔCBF. To address this issue, we designed our study to achieve significant ΔBOLD during both CALC and MEM tasks in identical voxels, which allows the within-voxel comparisons of ΔBOLD and quantitative parameters. Across only these voxels (Fig. S1H, 'conjunction voxels'), we again observed only weak ΔCBF (-0.5%) for negative ΔBOLD, but a strong positive ΔCBF (5.9%) for positive ΔBOLD, despite comparable positive and negative ΔBOLD amplitudes (-0.29% and 0.32%). At least for this subset of voxels, a discordant negative ΔBOLD is unlikely caused by voxel-specific artifacts, as we did observe a canonical hemodynamic response for positive but not negative BOLD signal changes.

In summary, we identified a canonical hemodynamic response for positive ΔBOLD across the cortex, yet with specific regions displaying a discordant BOLD signal response. For negative ΔBOLD, we did not find any significant ΔCBF or ΔCMRO2. Our findings across regions of the

human cortex match earlier studies in animals that reported inconsistent hemodynamic responses in cortical compared to subcortical regions (Huo et al., 2014; Shaw et al., 2021; Shih et al., 2011).

Validation of discordant hemodynamics using a hemodynamic response model and data from a replication study

On the level of voxels, we evaluated our findings in comparison to a well-established model of cerebral hemodynamic responses (Fig. 3). The Davis model predicts the amplitudes of BOLD signal changes for realistic ranges of ΔCMRO2 and associated ΔCBF in the human brain (Davis et al., 1998). Although published more than two decades ago, no study has examined the model's accuracy across the human cortex using BOLD fMRI and quantitative fMRI data. Intriguingly, the Davis model predicts a range of discordant positive and negative ΔBOLD for biologically plausible ΔCBF in relation to ΔCMRO2 (Fig. 3, violet shadings and voxels). Our empirical data (Fig. 3B) closely align with the predictions of the Davis model using model parameters from the literature. Across all voxels with concordant positive and negative ΔBOLD, we found a canonical hemodynamic response with an average *n*-ratio of 2.0 and 1.6, respectively (Fig. 3D). Importantly, our data also confirm the occurrence of a substantial amount of discordant voxels, accounting for 31% among CALC-positive and 66% of CALC-negative voxels in CALC vs. CTRL (Fig. 3C). We also validated the presence of discordant voxels in comparison to REST (Fig. S3A) and for the MEM condition (Fig. S3B). Furthermore, we applied the Davis model using parameters derived from our own data to calculate ΔCMRO2. This approach allowed us to replicate our main finding using Fick's principle resulting in a similar percentage and regional distribution of discordant voxels, and a comparable range of CMRO2 responses (Fig. S8). In summary, these results provide independent support for the robustness of the mqBOLD approach, and we successfully validated the model parameters of the Davis model established several decades ago.

Yet, one could argue that voxels with discordant ΔBOLD simply emerge from misalignment and partial volume effects when integrating voxel data from different modalities. Thus, we conducted a replication study with matching voxel sizes and matrices across BOLD- and mqBOLD sequences and with a higher voxel resolution in pCASL imaging, yet with the drawback of losing whole-brain coverage. Using the identical analysis pipeline of the main study, we again found an *n*-ratio > 1 for concordant voxels (BOLDpos/neg: 1.7/1.2) and, most crucially, a substantial amount of discordant voxels (BOLDpos/neg: 40%/40%) (Fig. S6).

One could also argue about sensitivity issues of mqBOLD across cortical voxels. For example, weak ΔCBF due to low pCASL sensitivity or dominance of vascular effects (high R2' or CBV) might artificially induce discordant ΔBOLD. We, therefore, validated our results using control masks including only significant ΔCBF or significant ΔCMRO2 voxels, instead of ΔBOLD, and excluding voxels with high vascular contribution (Fig. S7). All control analyses confirmed the presence of discordant voxels for both positive (range of all control analyses: 11-29%) and

negative (68-78%) ΔBOLD. Moreover, the Davis model relies on several parameters related to hemodynamics and MR-susceptibility (α, β), which influence the model's outcome (see Methods section). Yet, the original paper's sensitivity analyses indicate that their impact on the overall results of the model is "small, on the order of our standard error of measurement for a single subject" (Davis et al., 1998, page 1835).

As a final control against voxel-specific artifacts, we investigated the hemodynamic and metabolic response for both signs of ΔBOLD occurring within the same voxels (Fig. 4A, conjunction mask). We analyzed the response patterns in each of around 4.000 voxels and categorized them according to their response type. The 'concordant only' voxels displayed a canonical hemodynamic response for both positive and negative ΔBOLD, indicating that the mqBOLD method effectively detects a canonical hemodynamic response across the entire range of ΔBOLD. The largest group, termed 'mixed' voxels, exhibited a canonical hemodynamic response for positive ΔBOLD (Fig. 4B, red) but did not show a significant CBF response for negative ΔBOLD (Fig. 4B, orange). Paradoxically, based on BOLD fMRI data alone, one would interpret activity as increased in one condition and decreased in the other, despite those voxels showing a significant increase in ΔCMRO2 of similar amplitude in both tasks (Fig. 4B red/orange bar plots).

In summary, mqBOLD is a valid approach to detect canonical hemodynamic responses. Yet, we found a substantial number of voxels with discordant ΔBOLD across different tasks and compared them to different baseline conditions. Discordant voxels occurred for both positive and negative ΔBOLD as well as for ΔCMRO2 calculated via either Fick's formula or the Davis model, arguing against a sensitivity issue of the mqBOLD approach to detect negative hemodynamics. Moreover, we observed concordant and discordant responses within the same voxels, which argues against voxel-specific issues such as vascularization or partial volume effects. Together, this suggests that different hemodynamic mechanisms serve an increased demand for oxygen, as discussed previously. Shaw et al. reported microvascular differences in the rodent hippocampus, which may explain different neurovascular coupling in cortical and subcortical regions (Shaw et al., 2021). In humans, Devi et al. (2022) and Mullinger et al. (2014) both found discrepancies in the coupling of CBF and BOLD signal changes in sensory cortices, which they interpreted as different neurovascular coupling mechanisms, especially for negative ΔBOLD.

Baseline OEF indicates baseline metabolism and a second type of hemodynamic response during task conditions

According to Fick's principle, a ΔCMRO2 without a contribution of ΔCBF emerges from ΔOEF. We thus hypothesized different baseline OEF across voxels of varying hemodynamic response types, indicative of different oxygen buffers. Confirming this hypothesis, we found significantly different baseline OEFs across the three response types of the 'conjunction voxels' (Fig. 4C). Specifically, baseline OEF was lowest for 'discordant only' voxels and highest for 'concordant

only' voxels, with 'mixed' voxels in-between. We then examined baseline hemodynamics across the entire cortex and separately for concordant and discordant voxels across all tasks of our study, which account for 32% and 21% of all GM voxels, respectively (Fig. 5A). Across the range of baseline CMRO2 of all group of voxels, we found a significant positive linear relationship with CBF and OEF (Fig. 5A, scatter plots). Further, multiple linear regression analyses indicated that the majority of regional CMRO2 variability is explained by OEF (>68%), followed by CBF (>28%) and CBV (>1%). Replicating the result from the subset of 'conjunction voxels', we observed a significantly lower CBF and OEF in discordant compared to concordant voxels (Fig. 5B). We also confirmed the differences in baseline OEF and CBV using separate data from quantitative susceptibility mapping (Huck et al., 2019; Lüsebrink et al., 2021) (Fig. 5C). Together, this suggests that OEF is the most prominent modulator of baseline metabolism across the human cortex, and potentially indicative of the type of hemodynamic response during task conditions.

Finally, we specifically tested the contribution of OEF in accommodating CMRO2 at baseline and during task conditions in both concordant and discordant voxels (Fig. 5D). Similar to the results during baseline, a multiple linear regression analysis revealed that ΔOEF is the major factor (58% of the total explained variance) in accommodating task-related oxygen consumption across discordant voxels. On the other hand, concordant voxels predominantly accomodate ΔCMRO2 via ΔCBF (87%), underpinning the canonical hemodynamic response in these voxels. This suggests that OEF is the most predictive factor for baseline metabolism across the cortex and implies that ΔOEF is a major contributor to changing oxygen demands in a significant group of voxels across the human cortex. Our findings are consistent with rodent data, which have shown different patterns of neurovascular coupling based on variations in vascular composition (Ances et al., 2008; Boorman et al., 2010; A. Ekstrom, 2010; Shaw et al., 2021).

Systematic limitations of mqBOLD and control analyses

Although the mqBOLD approach is more available and less invasive than PET, it does have several limitations. It is important to note that any systematic biases in the quantification of CBF, OEF, and CMRO2 would only impact across-subject comparisons but cannot explain task effects, as those are calculated as ΔOEF or ΔCMRO2 within the same voxels.

Absolute CBV quantification using DSC MRI is hardly possible, and it reflects total rather than venous CBV. Yet, the limitation of measuring total CBV applies to nearly all other CBV measurements in humans, such as PET (Enmi et al., 2004). To make CBV values comparable across subjects, we employed a global normalization procedure (Hirsch et al., 2014). Additionally, we followed the recommendations of our institution's Ethical Board, restricting the application of contrast agent for DSC measurements to a maximum of one clinical dose per healthy participant. As a result, we acquired CBV during CTRL in all subjects and ΔCBV in a subset of subjects using two half-dose applications during CALC and CTRL, which has been

shown to yield reliable results (Hedderich et al., 2019). Despite these limitations, our CBV data are valuable as we are unaware of any other study attempting to quantify baseline CBV and ΔCBV during task processing in healthy subjects.

We also studied the sensitivity of our mqBOLD approach to reliably detect positive and negative ΔCBF. We replicated the amplitude and extent of decreased CBF of an earlier PET study (Fig. S2B) using a comparable analysis approach (Shulman, Corbetta, et al., 1997, S. 19). Moreover, our data demonstrate ΔCBF within regions of significant ΔBOLD, consistent with previous studies of MR-based CBF measurements (Jog et al., 2016; J. Kim et al., 2006; Qihong Zou et al., 2011).

Furthermore, CMRO2 values from white matter (WM) cannot be interpreted since T2 and T2* quantification are strongly influenced by orientation effects of myelinated nerve fibers within WM and differences in lipid concentration between GM and WM. Moreover, T2* values may be biased by magnetic background field gradients, particularly in frontobasal and temporal brain areas. In previous work, our group has carefully investigated these sources of systematic errors in OEF, particularly regarding the influence of background magnetic fields (Hirsch et al., 2014; Hirsch & Preibisch, 2013), T2-related bias (Kaczmarz, Hyder, et al., 2020), and orientation-related effects in WM structures and error propagation (Kaczmarz, Göttler, et al., 2020). Based on these studies, we are confident that mqBOLD fMRI allows for proper investigation of GM OEF and CMRO2, even though the presence of pial veins may still bias estimates of both mqBOLD and BOLD signals. Additionally, we applied proper masking to reduce partial volume effects of adjacent WM structures. Furthermore, we have recently demonstrated that mqBOLD-based OEF in GM agreed reasonably well with PET-based OEF (Kufer et al., 2022).

We also performed several control analyses to verify the study design. In the main study (Fig. 1), block durations varied for BOLD (30 sec) and quantitative (approx. 6 min) fMRI to achieve the best SNR for each modality. In a separate control study, we investigated the BOLD signal's stability across three minutes of task performance (Fig. S2D). For both positive and negative ΔBOLD, we identified stable levels of the BOLD signal across the entire period of continuous task performance of CALC and MEM. Similarly, we found sustained levels of the CBF signal across 6 min of task performance (Fig. S2E). Importantly, neither signal showed signs of habituation or drift effects across several minutes of acquisition.

Implications for the interpretation of BOLD fMRI and outlook

The discordant response type challenges the interpretation of the BOLD signal in relation to changes in neuronal activity and metabolism. In particular, negative ΔBOLD in areas with low baseline OEF may indicate increased neuronal activity and vice versa. As a solution, we recommend interpreting ΔBOLD in terms of neuronal activity only if CMRO2, or at least CBF data, are available for the same voxel and condition. In general, we propose quantitative BOLD

fMRI as a more precise tool to identify regional changes in neuronal activity across the cortex. Moreover, mqBOLD methods might elucidate differences in hemodynamic status or dynamics across cohorts with known differences in vasculature, such as in healthy aging or patients with stroke or AD.

Our study offers new insights into the regional distribution of hemodynamic changes and suggests varying mechanisms across the human cortex. Firstly, voxels regulating mainly through ΔOEF appear to have a greater oxygen buffer, meaning the oxygen pressure remains sufficiently high during task engagement (Leithner et al., 2010; Leithner & Royl, 2014). Secondly, the OEF-based regulation may be linked to different signaling mechanisms, such as astrocytic activity (Takata et al., 2018), shifts in excitatory/inhibitory signaling (Buxton et al., 2014; Uhlirova et al., 2016), or neuromodulatory regulation (Koush et al., 2021). Thirdly, our findings support the necessity of quantitative mqBOLD fMRI for future research. Quantitative BOLD is particularly valuable for studying subject groups with potentially altered hemodynamics, such as during aging (Tsvetanov et al., 2020) or in neurodegenerative disorders (Chen et al., 2022b), as changes in hemodynamics can significantly impact the interpretation of the BOLD signal (Archila-Melendez, M., 2020).

METHODS

Participants

Main study: We acquired data from 47 healthy human subjects, seven of whom had to be excluded because of a) apparent behavioral task difficulties (n=1), b) problems with contrast-agent application (n=2), or c) data quality problems (n=4) such as severe motion artifacts in CBF or R2' data, unilateral CBF data, or susceptibility artifacts, leaving us with a cohort of 40 healthy subjects (22 women, 18 men; mean age 32.1 ± 9.2y, all right-handed) for further analyses. While 30 of these subjects participated in all four conditions (CALC, MEM, CTRL, REST; design below), 10 subjects only performed CALC and CTRL conditions but additionally received two DSC scans during CALC and CTRL, which allows for a within-subject calculation of ΔCBV. This means that any analysis of MEM or REST only includes 30 datasets.

Control study: To investigate the stability of BOLD fMRI during extended periods of task performance, we performed BOLD fMRI of an independent cohort with 18 healthy subjects (control sample: 11 women, 7 men; mean age 28.1 ± 4.8y, all right-handed).

Replication study: To replicate the main study with identical analysis pipelines but with imaging data of matching voxel matrices and resolution across BOLD- and mqBOLD sequences, we acquired additional data from 10 healthy subjects (5 women, 5 men; mean age 31.8y ± 6.8y) performing CALC and CTRL.

All participants gave informed written consent to procedures approved by the Ethics Review Board of the Klinikum Rechts der Isar, Technical University of Munich.

Task design

Participants were lying in the scanner in a supine position and watched the task instructions on a screen positioned behind the scanner via a mirror mounted to the head coil. Right-hand responses were collected via a button box (fORP 932, 4 Buttons, Cambridge Research Systems). Before entering the scanner, we explained all task conditions to the participants, emphasizing staying concentrated and giving correct responses rather than being fast. Before entering the scanner, participants performed a short test run of each condition on a computer outside the scanning room. All tasks were programmed to continuously engage subjects throughout the functional imaging runs of BOLD and mqBOLD fMRI.

CALC (calculation task): The CALC condition was designed to evoke negative BOLD responses in the DMN and positive BOLD responses in a task-positive network, including frontoparietal and dorsal attention networks (DAN). During CALC, participants continuously solved arithmetic tasks in a self-paced manner with a maximum response time of 10 seconds per task, similar to the design by Lin and colleagues (Lin et al., 2011b). Specifically, a row of three numbers plus a question mark (n1, n2, n3, ?) was presented with the instruction to solve the arithmetic and fill in the missing number for ? using the button box (see Fig. 1A). The solution was based on the following rule: n2 - n1 = DIFF, n2 = n1+(1*DIFF), n3 = n2+(2*DIFF), therefore ? = n3+(3*DIFF). An exemplary row is 33 38 48 ?. Here, DIFF = 5; n2 = 38 (33 + 5), n3 = 48 (38 + 2*5) and ? = 63 (48 + 15). The participants saw three response options, including the correct answer, each assigned to a button on the response box.

MEM (autobiographical memory task): The MEM condition was based on the task design of Spreng and colleagues (DuPre et al., 2016; Spreng & Grady, 2010), where participants were asked to remember a specific event in the past given a cue picture. We aimed to match the

visual input across all three tasks, thus using a cue-word instead of a cue-picture. Participants were asked to recall as many details of any past event that came to their minds. The cue-word was shown for a maximum of 15 seconds. To measure the average time it took participants to recall and gauge the ease of memory retrieval, they were instructed to press the first button twice as soon as an event came to mind. If they could not recall any event or further details, they were asked to press the second and third buttons in succession to prompt a new cue word. We utilized this double-button pressing instruction to ensure consistency in the total number of button presses across all tasks.

CTRL (low-level baseline): The CTRL condition involved a task with low-level cognitive and attentional demands. A row of random letters was displayed for a set time between 5.9 and 8.9 seconds. The participants had to press a button to indicate whether the first letter was a vowel. We used CTRL as an active baseline, ensuring that the visual input and button presses were similar to those in the CALC and MEM tasks. While studies investigating DMN activations usually used a matched control task to calculate task contrasts (Addis et al., 2007; Burianova et al., 2010; Burianova & Grady, 2007b), studies investigating DMN deactivations (i.e., negative BOLD responses) typically compare them to an uncontrolled resting state baseline (Lin et al., 2011b; Pfefferbaum et al., 2011; Raichle et al., 2001).

REST (resting state baseline): To replicate those two types of DMN contrasts, we also acquired REST data where a white fixation cross was presented on a black screen, and participants were instructed to fixate the cross throughout scanning.

MRI acquisition parameters

MRI of the main study was performed on an Elition upgrade of a 3T Philips Ingenia MR scanner (Philips Healthcare, Best, The Netherlands). The control study was conducted on a different 3T Philips Ingenia MR scanner, both using a 32-channel head coil. Multi-parametric, quantitative BOLD MRI included the following sequences:

A) Multi-echo spin-echo T2 mapping**:** 3D gradient spin echo (GRASE) readout as described previously by our group (Kaczmarz et al. 2020) with 8 echoes of even-spaced echo times (TE): TE1 = ΔTE = 16ms; TR=251; readout duration = 128ms; α=90°; voxel size 2x2x3.3mm^3; 35 slices (30 slices in 4 subjects); total acquisition time = 2:28min (for 35 slices).

B) Multi-echo gradient-echo T2* mapping, as described previously by our group (Hirsch et al., 2014; Kaczmarz, Hyder, et al., 2020): 12 echoes, TE1 = ΔTE = 5ms; TR=2229ms; readout duration = 60ms; α=30°; voxel size 2x2x3mm^3; gap 0.3mm; 35 slices (30 slices in 4 subjects). Correction for magnetic background gradients with a standard sinc-Gauss excitation pulse (Baudrexel et al., 2009; Hirsch & Preibisch, 2013); acquisition of half- and quarter-resolution data in k-space center for motion correction (Nöth et al., 2014); total acquisition time = 6:08min (for 35 slices).

C) Pseudo-continuous arterial spin labeling (pCASL): following Alsop et al. (2015) and as implemented by our group (Göttler et al., 2019; Kaczmarz, Hyder, et al., 2020). Post-labeling delay 1800ms, label duration 1800ms; 4 background suppression pulses; 2D EPI readout; TE=11ms; TR=4500ms; α=90°; 20 slices (16 slices in one subject); EPI factor 29; acquisition voxel size 3.28x3.5x6.0mm^3; gap 0.6mm; 39 dynamics plus one proton density-weighted M0 scan; total acquisition time = 6:00min.

D) Dynamic susceptibility imaging (DSC), as described previously by our group (Hedderich et al., 2019): Single-shot GRE-EPI; EPI factor 49; 80 dynamics; TR = 2.0s; α=60°; acquisition voxel size 2x2x3.5mm^3; 35 slices (30 slices in 4 subjects). Injection of gadolinium-based contrast agent as a bolus after 5 dynamics, 0.1ml/kg, minimum 6ml, maximum 8ml per injection, flow rate: 4ml/s, additionally flushing with 25ml NaCl; total acquisition time = 2:49min (for 35 slices).

Additionally to mqBOLD sequences, we acquired

F) BOLD-fMRI using single-shot EPI, EPI factor 43; voxel size = 3.0x3.0x3.0mm^3; FOV 192x192x127.8mm^3; TE=30ms; TR=1.2s; α=70°; 40 slices; SENSE-factor = 2; MB-SENSE-factor = 2. 400 dynamics (8:05 min) for four conditions, 200 dynamics (4:05 min) for two conditions, 1650 dynamics (33:05 min) for the long-block control study acquisition. For susceptibility correction, a B0 field map was acquired with two echoes; TR/TE1/TE2=525ms/6.0ms/9.8ms; 40 slices; parallel acquisition; α=60°; voxel size = 3.0x3.0.3.0mm^3; FOV 192x192x127.8mm^3; total acquisition time: 0:35s.

G) T1-weighted 3D MPRAGE pre- and post-gadolinium (TI/TR/TE/α = 100ms/9ms/4ms/8°; CS-SENSE-factor=7.5; 170 slices; FOV=240x252x170 mm^3; voxel size 1.0x1.0x1.0mm^3; acquisition time=2:05min) and T2-weighted 3D FLAIR (fluid-attenuated inversion recovery; TR/TE/α = 4800/293/40°; CS-SENSE-factor=10; 140 slices; FOV=240x248.9x168mm^3; acquisition voxel size 1.2x1.2x1.2mm^3; turbo spin-echo factor 170; inversion delay 1650ms; acquisition time=2:09min) images were acquired for anatomical reference and to exclude brain lesions.

Imaging for the control study included T1-weighted 3D MPRAGE and BOLD-fMRI, all acquisition parameters identical to those described above.

The imaging parameters for the replication study with matching voxel matrices were:

T1-weighted 3D MPRAGE, multi-echo spin-echo T2 mapping and multi-echo gradient-echo T2* mapping as described above (T2/T2* voxel size = 2x2x3.3mm^3). BOLD-fMRI was acquired as described above, yet with a voxel acquisition size = 4x4x3mm^3, gap 0.3mm, 40 slices. PCASL was acquired as described above, yet with the same voxel size as BOLD fMRI (4x4x3mm^3, gap 0.3mm; 26 slices). This results in subject data acquired with harmonized voxel dimensions of identical BOLD/pCASL voxel sizes and four T2/T2* voxels per BOLD voxel in the x/y-plane. Please note that whole-brain coverage was not possible with this higher-resolution pCASL sequence. We, therefore, placed the volume with identical angulation to the other sequences and covered all main regions of interest from our main study (see 'brain coverage,' Fig. S6).

Data acquisition

After giving informed written consent, a medical doctor placed a venous catheter into the forearm, and blood samples were taken to measure hemoglobin, hematocrit (Hct), and creatinine values. Contrast agent for DSC measurements was only applied if creatinine values were normal to ensure healthy kidney function. Arterial oxygen saturation was measured via a pulse oximeter (Nonin 7500FO, Nonin Medical B.V., The Netherlands).

Main study: Please find an illustration of the imaging session of the main study in Fig. 1B.

BOLD fMRI: All four task conditions were presented using a 30s-block-design with four repetitions per condition, the four conditions randomized within each repetition block (400 dynamic scans plus two dummy scans, total acquisition time: 8:05min). We also acquired continuous resting-state BOLD fMRI data (500 dynamics, total acquisition time: 10:05min) that have not been used so far.

Across subjects, the entire BOLD-fMRI run was alternated with the mqBOLD fMRI runs to balance potential habituation or fatigue effects. During mqBOLD imaging, conditions were presented in pseudo-randomized order for pCASL and T2* mapping. One T2 mapping (CTRL) was also included to account for stable tissue properties during mqBOLD calculation. DSC (CTRL) and T1w post-gadolinium scans were performed at the end of the imaging session to avoid signal artifacts from the contrast agent in any other sequence. The contrast agent was administered through a venous catheter via a dedicated pump (Accutron MR, Medtron AG, Saarbrücken, Germany) in the presence of a medical doctor.

To gain insight into their performance during the MEM condition, participants were asked to complete a memory questionnaire after the imaging session. They had to indicate how easy they found it to recall concrete events of the MEM task on a difficulty scale (1='very easy', 2='rather easy', 3='rather difficult', 4='very difficult') and how detailed their memories were overall on a concreteness scale (1='very detailed', 2='rather detailed', 3='rather vague', 4='very vague'). On average, people scored 1.8 +/- 0.7 on the difficulty scale and 2.0 +/- 0.6 on the concreteness scale. This indicates that, on average, it was relatively easy for the subjects to recall a concrete event, and the memories were rather detailed. This was consistent with the reaction times, as it took participants, on average, only 2.5 ± 1s to recall an event.

A subsample of N=10 subjects from the main study performed only the CALC and CTRL conditions but additionally received two DSC scans (two half-doses of contrast agent, totaling a full clinical dose of maximally 16ml). This allowed us to calculate within-subject ΔCBV of task effects in this subsample.

Control study: Here, we acquired fMRI BOLD data using a 30s-block-design with CALC and MEM tasks (4 repetitions each, interleaved with CTRL blocks) and during extended, 3 min-task blocks of CALC and MEM (4 repetitions each, interleaved with 1min CTRL blocks). This resulted in a total scan time of 41 minutes.

Replication study: This study aimed to replicate the results of the main study with matching voxel matrices and resolution across sequences. We acquired structural T1w, T2, and T2* mapping as described above. BOLD fMRI and pCASL data were acquired with identical voxel resolution. BOLD fMRI task data were again acquired during all four conditions, CBF data during CALC and CTRL. We did not inject a contrast agent and, therefore, did not acquire CBV data. For the CBV data, we used the main study's group-median maps for CALC and CTRL.

Image processing

Processing of BOLD fMRI data

BOLD fMRI data were pre-processed running fMRIPrep 20.2.4 (Esteban, 2019) in a docker container based on Nipype 1.6.1 (Gorgolewski et al., 2011). This includes the following preprocessing steps: segmentation, estimation of motion parameters and other confounds, correction for susceptibility distortions, co-registration in native T1w space, and normalization

to MNI152-ICBM-2mm space with a non-linear 6th generation registration model developed by (Montreal Neurological Institute, McGill University). fMRIPrep relies on FSL 5.0.9 (Jenkinson et al., 2012; Smith et al., 2004) to register EPI time-series data to T1w data with boundary-based registration (BBR), FSL FAST for brain tissue segmentation, and ANTs 2.3.3 (Avants et al., 2008) for spatial normalization to MNI space in a multiscale, mutual-information based, nonlinear registration scheme, where all transforms are first concatenated and registration steps applied at once. As part of the fMRIPrep pipeline (Jenkinson et al., 2012; Smith et al., 2004), correction for head motion and susceptibility distortions were performed in each subject's native space by applying a single composite transform to the BOLD-fMRI time series. The same data were also resampled into standard space, generating a preprocessed BOLD run in MNI152NLin6Asym space. These preprocessed BOLD fMRI data, without global signal regression, were then used as an input for the PLS model. Processing of BOLD fMRI data was identical for all data from the main, control and replication study.

Calculation of quantitative parameter maps from mqBOLD data

We calculated all quantitative parameter maps using in-house scripts (in Matlab) and SPM12 (Wellcome Trust Centre for Neuroimaging, UCL, London, UK). Fig.1 illustrates the procedure and shows subject-averaged parameter maps, calculated as subject median across total GM. Tissue masks and artifact areas were defined and calculated in native space (see below) separately for each condition.

T2/T2*-mapping: Quantitative T2 and T2* parameter maps are obtained by applying mono-exponential fits to the multi-echo spin and gradient echo data, as described previously by our group (Hirsch et al., 2014; Kaczmarz, Hyder, et al., 2020; Preibisch et al., 2008). Corrections for macroscopic magnetic background fields (Hirsch & Preibisch, 2013) and motion were applied, the latter by redundant acquisitions of k-space centers (Nöth et al., 2014).

R2' maps are calculated via

$$R2' = \frac{1}{T2*} - \frac{1}{T2} \qquad [1]$$

yielding the transverse, reversible relaxation rate that depends on the vascular dHb content in a voxel (Blockley et al., 2013, 2015; Bright et al., 2019). Caution needs to be applied when interpreting these values at air-tissue boundaries (magnetic field inhomogeneities) or in deep GM (iron deposition) or WM structures (orientation effects in myelin), as discussed previously (Hirsch & Preibisch, 2013; Kaczmarz, Hyder, et al., 2020).

CBV is derived from DSC MRI after contrast agent application via full integration of leakage-corrected ΔR2*-curves (Boxermann, J.L., Schmainda, K.M., Weisskoff, R.M., 2006) and subsequent normalization to a white matter value of 2.5% (Leenders et al., 1990). The DSC procedure has been described previously by our group (Hedderich et al., 2019; Kluge et al., 2016).

OEF is calculated from R2' and CBV parameter maps via the mqBOLD approach (Christen et al., 2012; Yablonskiy & Haacke, 1994) and, as previously implemented by our group (Hirsch et al., 2014) via

$$OEF = \frac{R2'}{c \cdot CBV} \qquad [2]$$

with $c = \gamma \cdot \frac{4}{3} \cdot \pi \cdot \Delta\chi_0 \cdot hct \cdot B_0$, and specific parameters for the gyromagnetic ratio $\gamma = 2.675 \cdot 10^8\ s^{-1}\ T^{-1}$, the susceptibility difference between fully deoxygenated and oxygenated hemoglobin of $\Delta\chi_0 = 0.264 \cdot 10^{-6}$, the magnetic field strength $B_0 = 3T$ and the small-vessel hematocrit *hct*, which is calculated as 85% of the empirically measured (large-vessel) hematocrit values of each subject (Eichling et al., 1975; Hirsch et al., 2014).

CBF maps were calculated from pCASL data as described in (Alsop et al., 2015). Specifically, CBF is calculated as the pairwise differences of the averaged and motion-corrected label and control images and scaled by a proton-density weighted image.

CMRO2: For each condition separately, we then calculated the voxel-wise CMRO2 by combining all parameter maps via Fick's principle:

$$CMRO2 = OEF \cdot CBF \cdot C_aO_2 \qquad [3]$$

where C_aO_2 is the oxygen-carrying capacity of hemoglobin and was calculated as $C_aO_2 = 0.334 \cdot Hct \cdot 55.6 \cdot O_2sat$, with O_2sat being the oxygen saturation measured by a pulse oximeter (Bright et al., 2019; Ma et al., 2020). The C_aO_2 parameter reflects the arterial oxygen content (in µmol) for each subject, based on empirical data regarding Hct and arterial oxygen saturation. The OEF (in %) indicates how much oxygen is extracted during the passage of blood from cerebral arteries to veins. Along with CBF (in ml/100g brain tissue/min), these three parameters define the cerebral rate of oxygen consumption. During task states, both higher oxygen extraction and increased CBF can serve to accomodate a higher rate of oxygen consumption. All parameter maps were calculated in subject space and co-registered to the first echo of the T2 data. Any normalization into MNI space was performed afterward. Specifically, all mqBOLD parameter maps were first co-registered to native T1w space before applying the normalization matrix to MNI space, as derived from fMRIPrep. CBF values were upscaled by 25% to account for the systematic underestimation of CBF due to the four background suppression pulses, as motivated here (Garcia et al., 2005; Mutsaerts et al., 2014). The data of the replication study were processed identically to those of the main study.

Artifact correction and GM masking

To exclude voxels from artifact-affected brain areas, we calculated the temporal signal-to-noise ratio (tSNR) from the BOLD fMRI data per subject and voxel and transformed individual masks into MNI space. We then created a conjunction mask on the group level, excluding voxels from the lowest 15th percentile of tSNR in over 66% of participants. These were mainly located in areas with strong susceptibility perturbations, i.e., fronto- and temporo-basal brain areas. Additionally, we masked out the cerebellum and voxels with a GM probability < 0.5. The resulting group mask was applied to the output of the GLM group analysis and the input matrices for the partial least squares analyses. For the analyses in native space, we additionally used native-space parameter maps to mask CSF-prone areas (T2 > 90ms), high-susceptibility areas (R2' > 9 s^{-1}), voxels with a high percentage of blood volume (CBV >10%, probably driven by larger veins/arteries) and voxels with biologically implausible values, such as T2' > 90ms, OEF > 0.9, and CBF > 90ml/100g/min.

Estimation of a realistic surrogate for CBV during CALC

During the evaluation of our study by the Ethics Board of the University Hospital, we agreed on using one typical clinical dosage of contrast agent as the maximum to measure CBV in healthy subjects. We, therefore, acquired DSC data during CTRL as a baseline measurement of CBV across the individual cortex. However, following a sensitivity analysis of another dataset at our institution, we learned that half the clinical dosage was enough to reliably evaluate CBV in healthy subjects. As a result, we collected two separate DSC datasets for the final subset of 10 subjects, each receiving two half dosages during CALC and CTRL, and allowing us to quantify CBV in both conditions.

From these measurements, we determined the voxel ΔCBV for CALC compared to CTRL in subject space and averaged it within 360 functional regions of interest (ROIs) as defined by (Glasser, 2016). We then calculated the median change per ROI across the 10 subjects to estimate ΔCBV for a template brain. Using this average ΔCBV map, we estimated a realistic CBV surrogate map during CALC for the remaining 30 subjects, for whom only one baseline CBV measurement was available. We used the CBV CTRL map to calculate the MEM condition, as no CBV measurements were available during MEM. To our knowledge, this is the most empirically based data used for ΔCBV in quantitative fMRI studies.

Semi-quantitative, BOLD-informed, CMRO2 estimation

The estimation of quantitative CMRO2 maps relies on the combination of R2', CBV, and CBF values, according to Eq. [3]. To control for potential error propagation during voxel-wise analyses, especially from R2' measurements (see appendix in (Kaczmarz, Göttler, et al., 2020), we calculated R2' parameter maps during MEM and CALC from baseline R2'- and BOLD fMRI data as suggested by Fujita et al. (2006). Instead of calculating ΔR2' from quantitative R2' (multi-echo GE-based T2*) during task conditions, ΔR2' is approximated as

$$\Delta R2' = -\frac{\Delta S}{S_0}\frac{1}{TE \cdot R2'_0} \qquad [4]$$

with TE = 30ms, $R2'_0$ being the baseline R2', and $\frac{\Delta S}{S_0}$ the BOLD signal change, derived from task data. R2' in CALC and MEM was calculated via $R2' = R2'_0 + (\Delta R2' \cdot R2'_0)$ and fed into OEF and CMRO2 calculations according to Eqs. [2] and [3]. Thus, these CMRO2 parameter maps in CALC and MEM differ from the regional CMRO2 maps only in their underlying R2' values. In Fig. S5, we plotted the PLS results from the BOLD-informed approach and found very similar signal ranges and voxel distributions.

Davis model

The Davis model was originally used for calibrated fMRI and is a simulation of ΔBOLD (= $\Delta S/S_0$) using carbon dioxide breathing as a physiological means of manipulating CBF independent of CMRO2 and relying on parameters M, α, and β (Davis et al., 1998):

$$\frac{\Delta S}{S_0} = M\left[1 - \left(\frac{CBF}{CBF_0}\right)^{\alpha-\beta}\left(\frac{CMRO2}{CMRO2_0}\right)^{\beta}\right] \qquad [5]$$

where α is a power-law exponent, relating CBV to CBF changes, and β depends on the microvascular anatomy (Bright et al., 2019). Previously, a value of α = 0.38 was used (Grubb et

al., 1974); however, lower values have recently been identified. In Fig. 3A, we plotted the range of expected ΔBOLD using empirical values for all parameters, which we derived from recent calibration studies with α = 0.23, β = 1.3 (Bright et al., 2019), and M=5.5 (Chen et al., 2022b). M is commonly referred to as the maximum ΔBOLD that occurs if all dHb is washed out of the vessels; it depends on baseline OEF (Blockley et al., 2013). For the calibration of fMRI experiments, M is estimated via combined measurement of CBF and BOLD responses to a vasoactive stimulus, mostly hypercapnia. Assuming α and β, the fractional change in CMRO2 can be calculated from combined BOLD signal and CBF measurements during tasks (Blockley et al., 2013; Chen et al., 2022b; Germuska & Wise, 2019).

We also performed a validation experiment where we estimated parameters M and α from our imaging data. This allowed us to directly compare ΔCMRO2 as calculated via the two most prominent approaches, Fick's formula in Eq. [3] and the Davis model in Eq. [5], solved for $CMRO2_{task}$. To this end, we analyzed the data from the control condition of N = 40 subjects in native space and extracted median values for the Glasser parcellation (Glasser et al., 2016). As described in Grubb et al. (1974), we assumed a power-law relationship between CBV and CBF: $CBV = 0.8\ CBF^{\alpha}$. Fitting this formula to our empirical data, using venousCBV = 0.7 * totalCBV, resulted in α = 0.38. We then calculated a subject-specific calibration factor M via M = TE * R2', with R2' based on venousCBV, resulting in an average M = 11.2 ± 1% across 40 subjects.

Statistics

Partial least squares analysis of BOLD and mqBOLD data

Partial least squares (PLS) analyses were performed using the pyls library in Python language (Python Software Foundation, version 3.8). Mean-centered PLS is a data-reduction method that computes latent variables and corresponding brain patterns, which optimally relate brain signals to the experimental design, contrasting, e.g., groups or conditions (McIntosh & Lobaugh, 2004). In our case, the input-data matrix to calculate a contrast of interest contained one row for each subject, including all voxels within the artifact-corrected mask (see above), stacked across conditions of interest, e.g., CALC and CTRL. In the case of BOLD fMRI data, median values of percent signal change (from either CTRL or REST) across 24s (20 TRs) per task condition were used, excluding the first 6s per task block to account for the hemodynamic response lag. For mqBOLD data, quantitative OEF, CBF, or CMRO2 values per voxel and subject were used for all conditions. With the help of a dummy-coding matrix, the pyls library computes within-condition averages, which are column-wise mean-centered (Krishnan et al., 2011). This matrix, $R_{mean\text{-}centered\ (q\ x\ p)}$, which comprises q conditions and p voxels, is then subjected to singular value decomposition, which results in:

$$R'_{mean\text{-}centered} = USV' \qquad [6]$$

where $U_{p\,x\,q}$ are the voxel weights (brain saliences), one row per latent variable (LV), that reflect how much this voxel contributes to the effect captured by LV_i. $V_{q\ x\ q}$ is the matrix of task saliences (one row per LV) that indicates how each condition contributes to the spatial pattern identified by LV_i. $S_{q\,x\,q}$ are the singular values per LV that reflect the strength of the relationship extracted by each LV_i (McIntosh & Mišić, 2013). The significance of the LVs, i.e., the entire multivariate pattern, was tested via permutation tests (3000 permutations), and the reliability of the brain saliences, i.e., the voxel's contribution to the LVs, was deduced via bootstrap resampling (3000 samples). Brain regions showing significant effects were identified via the

ratio of the brain saliences to the bootstrap standard error (BSR), where a BSR > ±2 is akin to a confidence interval of 95% if the bootstrap distribution is normal (Krishnan et al., 2011; McIntosh & Mišić, 2013). In this paper, we used PLS analyses to perform group-level statistics to identify brain regions that best differentiate between a task (CALC or MEM) and a baseline (CTRL or REST) condition. As the same analysis was applied to both BOLD fMRI and mqBOLD data, resulting statistical maps can be compared across the different parameters. The statistical maps in Fig. 2A and Fig. S1A and S1D were thresholded with a BSR of ±2, and only clusters with more than 30 voxels were kept for creating group masks. For correct interpretation, BSR maps must be compared to the design scores (design variables multiplied by brain saliences) of each condition within each LV to know the direction of task differences captured by the BSR pattern. In this manuscript, an orange-red BSR pattern indicates a positive task effect, that is, voxels with higher values during the task compared to the baseline, whereas blue voxels show the opposite contrast. In order to visualize the whole-brain, non-thresholded PLS results, we transformed the statistical maps from native to surface space, using the "vol_to_surf" function from nilearn's surface toolbox, and plotted the maps onto the "fsaverage pial left and right mesh" via the function "plot_surf_stat_mat".

BOLD clusters

The BOLD clusters shown in Fig. 2D are based on the PLS analysis of the BOLD data. Statistical maps were thresholded with a BSR > +/-3. Connected regions with a minimum region size of 1000 voxels were extracted using Nilearn's region package in Python. Then, upon visual inspection, clusters that apparently were fractionated by the algorithm but that belonged together based on Yeo's network templates (Thomas Yeo et al., 2011) were again fused.

General linear modeling of BOLD data

As a control for PLS analyses, we used a general linear model (GLM) approach for task analysis following recommendations (Esteban et al., 2020).

We set up a GLM with separate confound columns (CSF, WM signal, dvars, framewise displacement, translations/rotations in x-, y- and z-axis) and applied a high-pass filter of 100s and a 6mm smoothing kernel. For native-space analyses based on GLM masks, we used individual 1st-level z-maps, z > 2.5. The following contrasts were calculated: CALC-positive = CALC > CTRL or REST, CALC-negative = CALC < CTRL or REST, MEM-positive = MEM > CTRL, MEM-negative = MEM < CTRL. For the cross-validation of the PLS group results with a group-level GLM analysis, we used FWE-corrected z-maps from the 2nd level analysis.

CBF peak ROIs

To compare our data to CBF data generated from PET imaging, we used a similar approach described in the seminal paper by Shulman and colleagues (Shulman, FIEZ, et al., 1997). We calculated median ΔCBF[%] across subjects, with a threshold of CBF < -2% and without further corrections (Fig. S2B). CBF peak ROIs were derived from the PLS-derived statistical group map, as shown in Fig. S2B on the right. We used the atlasreader library in Python (Notter et al., 2019) to extract peak coordinates. We then selected the coordinates of nine (out of 15) peaks with

the highest positive peak values, plus all seven peaks with negative peak values, to create spheres with 5mm diameter around these coordinates. Median CBF and CMRO2 responses were extracted within these spheres to compare CALC versus REST conditions and to the original figure in the Shulman et al. paper.

Other statistical analyses

For the native space analyses, we calculated median values within each native-space ROI (output of the first level GLM, thresholded with z>2.5) per subject and tested significant differences in tasks compared to baseline via separate paired-samples, two-sided, t-tests, across subjects. All other statistics were based on median voxel values within a group mask in standard space by taking the across-subjects median value per voxel in task and baseline (Fig. 2B, Fig. 3B, Fig. 4A&D). Barplots showing median voxel values were generated via Python's seaborn library (Waskom, 2021), with error bars showing a 95% confidence interval (CI) using 2000 permutations. If the CI included zero, the median delta value was defined as statistically non-significant. To test differences in hemodynamics between discordant and concordant voxels, we used paired, two-sided t-tests on the median subject values; to test for baseline differences, we used independent-sample permutation tests on the median voxel values. External, high-resolution maps were downsampled to 2mm MNI standard space before analyses were conducted.

FUNDING

CP has been funded by the Deutsche Forschungsgemeinschaft (DFG, German Research Foundation, ID 395030489), and VR has been supported by the European Research Council (ERC) under the European Union's Horizon 2020 research and innovation program (ERC Starting Grant, ID 759659).

DATA and CODE AVAILABILITY

All raw and processed data are available in the online repository of OpenNEURO: https://openneuro.org/datasets/ds004873. The scripts, Python Jupyter notebooks, docker container for quantitative parameter map analyses, and configuration files for replication of all analyses and figures are available on GitHub: https://github.com/NeuroenergeticsLab/two_modes_of_hemodynamics.

REFERENCES

Addis, D. R., Wong, A. T., & Schacter, D. L. (2007). Remembering the past and imagining the future: Common and distinct neural substrates during event construction and elaboration. *Neuropsychologia*, *45*(7), 1363–1377. https://doi.org/10.1016/j.neuropsychologia.2006.10.016

Alsop, D. C., Detre, J. A., Golay, X., Günther, M., Hendrikse, J., Hernandez-Garcia, L., Lu, H., MacIntosh, B. J., Parkes, L. M., Smits, M., van Osch, M. J. P., Wang, D. J. J., Wong, E. C., & Zaharchuk, G. (2015). Recommended implementation of arterial spin-labeled perfusion MRI for clinical applications: A consensus of the ISMRM perfusion study group and the European consortium for ASL in dementia: Recommended Implementation of ASL for Clinical Applications. *Magnetic Resonance in Medicine*, *73*(1), 102–116. https://doi.org/10.1002/mrm.25197

Alzaidi, A. A., Panek, R., & Blockley, N. P. (2024). Quantitative BOLD (qBOLD) imaging of oxygen metabolism and blood oxygenation in the human body: A scoping review. *Magnetic Resonance in Medicine*, mrm.30165. https://doi.org/10.1002/mrm.30165

Amalric, M., & Dehaene, S. (2016). Origins of the brain networks for advanced mathematics in expert mathematicians. *Proceedings of the National Academy of Sciences*, *113*(18), 4909–4917. https://doi.org/10.1073/pnas.1603205113

An, H., & Lin, W. (2000). Quantitative Measurements of Cerebral Blood Oxygen Saturation Using Magnetic Resonance Imaging. *Journal of Cerebral Blood Flow & Metabolism*, *20*(8), 1225–1236. https://doi.org/10.1097/00004647-200008000-00008

Ances, B. M., Leontiev, O., Perthen, J. E., Liang, C., Lansing, A. E., & Buxton, R. B. (2008). Regional differences in the coupling of cerebral blood flow and oxygen metabolism changes in response to activation: Implications for BOLD-fMRI. *NeuroImage*, *39*(4), 1510–1521. https://doi.org/10.1016/j.neuroimage.2007.11.015

Andrews-Hanna, J. R., Saxe, R., & Yarkoni, T. (2014). Contributions of episodic retrieval and mentalizing to autobiographical thought: Evidence from functional neuroimaging, resting-state connectivity, and fMRI meta-analyses. *NeuroImage*, *91*, 324–335. https://doi.org/10.1016/j.neuroimage.2014.01.032

Anticevic, A., Cole, M. W., Murray, J. D., Corlett, P. R., Wang, X.-J., & Krystal, J. H. (2012). The role of default network deactivation in cognition and disease. *Trends in Cognitive Sciences*, *16*(12), 584–592. https://doi.org/10.1016/j.tics.2012.10.008

Aoe, J., Watabe, T., Shimosegawa, E., Kato, H., Kanai, Y., Naka, S., Matsunaga, K., Isohashi, K., Tatsumi, M., & Hatazawa, J. (2018). Evaluation of the default-mode network by quantitative 15O-PET: Comparative study between cerebral blood flow and oxygen consumption. *Annals of Nuclear Medicine*, *32*(7), 485–491. https://doi.org/10.1007/s12149-018-1272-x

Archila-Melendez, M. (2020). Modeling the impact of neurovascular coupling impairments on BOLD-based functional connectivity at rest. *NeuroImage*, *218*, 116871. https://doi.org/10.1016/j.neuroimage.2020.116871

Attwell, D., Buchan, A. M., Charpak, S., Lauritzen, M., MacVicar, B. A., & Newman, E. A. (2010). Glial and neuronal control of brain blood flow. *Nature*, *468*(7321), 232–243. https://doi.org/10.1038/nature09613

Avants, B., Epstein, C., Grossman, M., & Gee, J. (2008). Symmetric diffeomorphic image registration with cross-correlation: Evaluating automated labeling of elderly and

neurodegenerative brain. *Medical Image Analysis*, *12*(1), 26–41. https://doi.org/10.1016/j.media.2007.06.004

Baudrexel, S., Volz, S., Preibisch, C., Klein, J. C., Steinmetz, H., Hilker, R., & Deichmann, R. (2009). Rapid single-scan T2*-mapping using exponential excitation pulses and image-based correction for linear background gradients: T2* Mapping With Field Gradient Correction. *Magnetic Resonance in Medicine*, *62*(1), 263–268. https://doi.org/10.1002/mrm.21971

Bergel, A., Tiran, E., Deffieux, T., Demené, C., Tanter, M., & Cohen, I. (2020). Adaptive modulation of brain hemodynamics across stereotyped running episodes. *Nature Communications*, *11*(1). Scopus. https://doi.org/10.1038/s41467-020-19948-7

Blockley, N. P., Griffeth, V. E. M., & Buxton, R. B. (2012). A general analysis of calibrated BOLD methodology for measuring CMRO2 responses: Comparison of a new approach with existing methods. *NeuroImage*, *60*(1), 279–289. https://doi.org/10.1016/j.neuroimage.2011.11.081

Blockley, N. P., Griffeth, V. E. M., Simon, A. B., & Buxton, R. B. (2013). A review of calibrated blood oxygenation level-dependent (BOLD) methods for the measurement of task-induced changes in brain oxygen metabolism: A REVIEW OF CALIBRATED BOLD METHODS. *NMR in Biomedicine*, *26*(8), 987–1003. https://doi.org/10.1002/nbm.2847

Blockley, N. P., Griffeth, V. E. M., Simon, A. B., Dubowitz, D. J., & Buxton, R. B. (2015). Calibrating the BOLD response without administering gases: Comparison of hypercapnia calibration with calibration using an asymmetric spin echo. *NeuroImage*, *104*, 423–429. https://doi.org/10.1016/j.neuroimage.2014.09.061

Boorman, L., Kennerley, A. J., Johnston, D., Jones, M., Zheng, Y., Redgrave, P., & Berwick, J. (2010). Negative Blood Oxygen Level Dependence in the Rat:A Model for Investigating the Role of Suppression in Neurovascular Coupling. *Journal of Neuroscience*, *30*(12), 4285–4294. https://doi.org/10.1523/JNEUROSCI.6063-09.2010

Bouvier, J., Detante, O., Tahon, F., Attye, A., Perret, T., Chechin, D., Barbieux, M., Boubagra, K., Garambois, K., Tropres, I., Grand, S., Barbier, E. L., & Krainik, A. (2015). Reduced CMRO $_2$ and cerebrovascular reserve in patients with severe intracranial arterial stenosis: A combined multiparametric qBOLD oxygenation and BOLD fMRI study. *Human Brain Mapping*, *36*(2), 695–706. https://doi.org/10.1002/hbm.22657

Boxermann, J.L., Schmainda, K.M., Weisskoff, R.M. (2006). Relative Cerebral Blood Volume Maps Corrected for Contrast Agent Extravasation Significantly Correlate with Glioma Tumor Grade, Whereas Uncorrected Maps Do Not. *Amercian Journal of Neuroradiology*, *27*(4), 859–867.

Boynton, G. M. (2011). Spikes, BOLD, Attention, and Awareness: A comparison of electrophysiological and fMRI signals in V1. *Journal of Vision*, *11*(5), 12. https://doi.org/10.1167/11.5.12

Bright, M. G., Croal, P. L., Blockley, N. P., & Bulte, D. P. (2019). Multiparametric measurement of cerebral physiology using calibrated fMRI. *NeuroImage*, *187*, 128–144. https://doi.org/10.1016/j.neuroimage.2017.12.049

Burianova, H., & Grady, C. L. (2007a). Common and Unique Neural Activations in Autobiographical, Episodic, and Semantic Retrieval. *Journal of Cognitive Neuroscience*, *19*(9), 1520–1534. https://doi.org/10.1162/jocn.2007.19.9.1520

Burianova, H., & Grady, C. L. (2007b). Common and Unique Neural Activations in Autobiographical, Episodic, and Semantic Retrieval. *Journal of Cognitive Neuroscience*, *19*(9), 1520–1534. https://doi.org/10.1162/jocn.2007.19.9.1520

Burianova, H., McIntosh, A. R., & Grady, C. L. (2010). A common functional brain network for autobiographical, episodic, and semantic memory retrieval. *NeuroImage*, *49*(1), 865–874. https://doi.org/10.1016/j.neuroimage.2009.08.066

Buxton, R. B. (2010). Interpreting oxygenation-based neuroimaging signals: The importance and the challenge of understanding brain oxygen metabolism. *Frontiers in Neuroenergetics*. https://doi.org/10.3389/fnene.2010.00008

Buxton, R. B. (2020). The thermodynamics of thinking: Connections between neural activity, energy metabolism and blood flow. *bioRxiv*, 833855. https://doi.org/10.1101/833855

Buxton, R. B. (2023). *Thermodynamic limitations on brain oxygen metabolism: Physiological implications* [Preprint]. Neuroscience. https://doi.org/10.1101/2023.01.06.522942

Buxton, R. B., & Frank, L. R. (1997). A Model for the Coupling between Cerebral Blood Flow and Oxygen Metabolism during Neural Stimulation. *Journal of Cerebral Blood Flow & Metabolism*, *17*(1), 64–72. https://doi.org/10.1097/00004647-199701000-00009

Buxton, R. B., Griffeth, V. E. M., Simon, A. B., & Moradi, F. (2014). Variability of the coupling of blood flow and oxygen metabolism responses in the brain: A problem for interpreting BOLD studies but potentially a new window on the underlying neural activity. *Frontiers in Neuroscience*, *8*. https://doi.org/10.3389/fnins.2014.00139

Cardoso, M. M. B., Sirotin, Y. B., Lima, B., Glushenkova, E., & Das, A. (2012). The neuroimaging signal is a linear sum of neurally distinct stimulus- and task-related components. *Nature Neuroscience*, *15*(9), 1298–1306. https://doi.org/10.1038/nn.3170

Chen, J. J., Uthayakumar, B., & Hyder, F. (2022a). Mapping oxidative metabolism in the human brain with calibrated fMRI in health and disease. *Journal of Cerebral Blood Flow & Metabolism*, *42*(7), 1139–1162. https://doi.org/10.1177/0271678X221077338

Chen, J. J., Uthayakumar, B., & Hyder, F. (2022b). Mapping oxidative metabolism in the human brain with calibrated fMRI in health and disease. *Journal of Cerebral Blood Flow & Metabolism*, *42*(7), 1139–1162. https://doi.org/10.1177/0271678X221077338

Chiarelli, P. A., Bulte, D. P., Wise, R., Gallichan, D., & Jezzard, P. (2007). A calibration method for quantitative BOLD fMRI based on hyperoxia. *NeuroImage*, *37*(3), 808–820. https://doi.org/10.1016/j.neuroimage.2007.05.033

Cho, J., Kee, Y., Spincemaille, P., Nguyen, T. D., Zhang, J., Gupta, A., Zhang, S., & Wang, Y. (2018). Cerebral metabolic rate of oxygen ($CMRO_2$) mapping by combining quantitative susceptibility mapping (QSM) and quantitative blood oxygenation level-dependent imaging (qBOLD). *Magnetic Resonance in Medicine*, *80*(4), 1595–1604. https://doi.org/10.1002/mrm.27135

Christen, T., Schmiedeskamp, H., Straka, M., Bammer, R., & Zaharchuk, G. (2012). Measuring brain oxygenation in humans using a multiparametric quantitative blood oxygenation level dependent MRI approach. *Magnetic Resonance in Medicine*, *68*(3), 905–911. https://doi.org/10.1002/mrm.23283

Das, A., & Sirotin, Y. B. (2011). What could underlie the trial-related signal? A response to the commentaries by Drs. Kleinschmidt and Muller, and Drs. Handwerker and Bandettini. *NeuroImage*, *55*(4), 1413–1418. https://doi.org/10.1016/j.neuroimage.2010.07.005

Davey, C. G., Pujol, J., & Harrison, B. J. (2016). Mapping the self in the brain's default mode network. *NeuroImage*, *132*, 390–397. https://doi.org/10.1016/j.neuroimage.2016.02.022

Davis, T. L., Kwong, K. K., Weisskoff, R. M., & Rosen, B. R. (1998). Calibrated functional MRI: Mapping the dynamics of oxidative metabolism. *Proceedings of the National Academy of Sciences*, *95*(4), 1834–1839. https://doi.org/10.1073/pnas.95.4.1834

Devi, R., Lepsien, J., Lorenz, K., Schlumm, T., Mildner, T., & Möller, H. E. (2022). Multi-echo investigations of positive and negative CBF and concomitant BOLD changes. *NeuroImage*, *263*, 119661. https://doi.org/10.1016/j.neuroimage.2022.119661

Devonshire, I. M., Papadakis, N. G., Port, M., Berwick, J., Kennerley, A. J., Mayhew, J. E. W., & Overton, P. G. (2012). Neurovascular coupling is brain region-dependent. *NeuroImage*, *59*(3), 1997–2006. https://doi.org/10.1016/j.neuroimage.2011.09.050

Devor, A., Dunn, A. K., Andermann, M. L., Ulbert, I., Boas, D. A., & Dale, A. M. (2003). Coupling of Total Hemoglobin Concentration, Oxygenation, and Neural Activity in Rat Somatosensory Cortex. *Neuron*, *39*(2), 353–359. https://doi.org/10.1016/S0896-6273(03)00403-3

Devor, A., Hillman, E. M. C., Tian, P., Waeber, C., Teng, I. C., Ruvinskaya, L., Shalinsky, M. H., Zhu, H., Haslinger, R. H., Narayanan, S. N., Ulbert, I., Dunn, A. K., Lo, E. H., Rosen, B. R., Dale, A. M., Kleinfeld, D., & Boas, D. A. (2008). Stimulus-Induced Changes in Blood Flow and 2-Deoxyglucose Uptake Dissociate in Ipsilateral Somatosensory Cortex. *Journal of Neuroscience*, *28*(53), 14347–14357. https://doi.org/10.1523/JNEUROSCI.4307-08.2008

Devor, A., Tian, P., Nishimura, N., Teng, I. C., Hillman, E. M. C., Narayanan, S. N., Ulbert, I., Boas, D. A., Kleinfeld, D., & Dale, A. M. (2007). Suppressed Neuronal Activity and Concurrent Arteriolar Vasoconstriction May Explain Negative Blood Oxygenation Level-Dependent Signal. *Journal of Neuroscience*, *27*(16), 4452–4459. https://doi.org/10.1523/JNEUROSCI.0134-07.2007

DiNuzzo, M., Dienel, G. A., Behar, K. L., Petroff, O. A., Benveniste, H., Hyder, F., Giove, F., Michaeli, S., Mangia, S., Herculano-Houzel, S., & Rothman, D. L. (2023). Neurovascular coupling is optimized to compensate for the increase in proton production from nonoxidative glycolysis and glycogenolysis during brain activation and maintain homeostasis of pH, $p\,CO_2$, and $p\,O_2$. *Journal of Neurochemistry*, jnc.15839. https://doi.org/10.1111/jnc.15839

Drew, P. J. (2019). Vascular and neural basis of the BOLD signal. *Current Opinion in Neurobiology*, *58*, 61–69. https://doi.org/10.1016/j.conb.2019.06.004

Drew, P. J. (2022). Neurovascular coupling: Motive unknown. *Trends in Neurosciences*, *45*(11), 809–819. https://doi.org/10.1016/j.tins.2022.08.004

DuPre, E., Luh, W.-M., & Spreng, R. N. (2016). Multi-echo fMRI replication sample of autobiographical memory, prospection and theory of mind reasoning tasks. *Scientific Data*, *3*(1), 160116. https://doi.org/10.1038/sdata.2016.116

Eichling, J. O., Raichle, M. E., Grubb, R. L., Larson, K. B., & Ter-Pogossian, M. M. (1975). In vivo determination of cerebral blood volume with radioactive oxygen-15 in the monkey. *Circulation Research*, *37*(6), 707–714. https://doi.org/10.1161/01.RES.37.6.707

Ekstrom, A. (2010). How and when the fMRI BOLD signal relates to underlying neural activity: The danger in dissociation. *Brain Research Reviews*, *62*(2), 233–244. https://doi.org/10.1016/j.brainresrev.2009.12.004

Ekstrom, A. D. (2021). Regional variation in neurovascular coupling and why we still lack a Rosetta Stone. *Philosophical Transactions of the Royal Society B: Biological Sciences*, *376*(1815), 20190634. https://doi.org/10.1098/rstb.2019.0634

Engl, E., & Attwell, D. (2015). Non-signalling energy use in the brain. *The Journal of Physiology*, *593*(16), 3417–3429. https://doi.org/10.1113/jphysiol.2014.282517

Enmi, J., Hayashi, T., Watabe, H., Moriwaki, H., Yamada, N., & Iida, H. (2004). Measurement of cerebral blood flow with dynamic susceptibility contrast MRI and comparison with O-15 positron emission tomography. *International Congress Series*, *1265*, 150–158. https://doi.org/10.1016/j.ics.2004.04.045

Esteban, O. (2019). fMRIPrep: A robust preprocessing pipeline for functional MRI. *Nature Methods*, *16*, 14.

Esteban, O., Ciric, R., Finc, K., Blair, R. W., Markiewicz, C. J., Moodie, C. A., Kent, J. D., Goncalves, M., DuPre, E., Gomez, D. E. P., Ye, Z., Salo, T., Valabregue, R., Amlien, I. K., Liem, F., Jacoby, N., Stojić, H., Cieslak, M., Urchs, S., … Gorgolewski, K. J. (2020). Analysis of task-based functional MRI data preprocessed with fMRIPrep. *Nature Protocols*, *15*(7), 2186–2202. https://doi.org/10.1038/s41596-020-0327-3

Fan, A. P., Bilgic, B., Gagnon, L., Witzel, T., Bhat, H., Rosen, B. R., & Adalsteinsson, E. (2014). Quantitative oxygenation venography from MRI phase: Quantitative Oxygenation Venography. *Magnetic Resonance in Medicine*, *72*(1), 149–159. https://doi.org/10.1002/mrm.24918

Fehr, T., Code, C., & Herrmann, M. (2007). Common brain regions underlying different arithmetic operations as revealed by conjunct fMRI–BOLD activation. *Brain Research*, *1172*, 93–102. https://doi.org/10.1016/j.brainres.2007.07.043

Fleisher, A. S., Podraza, K. M., Bangen, K. J., Taylor, C., Sherzai, A., Sidhar, K., Liu, T. T., Dale, A. M., & Buxton, R. B. (2009). Cerebral perfusion and oxygenation differences in Alzheimer's disease risk. *Neurobiology of Aging*, *30*(11), 1737–1748. https://doi.org/10.1016/j.neurobiolaging.2008.01.012

Fox, P., & Raichle, M. E. (1986). Focal physiological uncoupling of cerebral blood flow and oxidative metabolism during somatosensory stimulation in human subjects. *Proceedings of the National Academy of Sciences*, *83*(4), 1140–1144. https://doi.org/10.1073/pnas.83.4.1140

Fox, P., Raichle, M., Mintun, M., & Dence, C. (1988). Nonoxidative glucose consumption during focal physiologic neural activity. *Science*, *241*(4864), 462–464. https://doi.org/10.1126/science.3260686

Fracasso, A., Gaglianese, A., Vansteensel, M. J., Aarnoutse, E. J., Ramsey, N. F., Dumoulin, S. O., & Petridou, N. (2022). FMRI and intra-cranial electrocorticography recordings in the same human subjects reveals negative BOLD signal coupled with silenced neuronal activity. *Brain Structure and Function*, *227*(4), 1371–1384. https://doi.org/10.1007/s00429-021-02342-4

Fujita, N., Matsumoto, K., Tanaka, H., Watanabe, Y., & Murase, K. (2006). Quantitative study of changes in oxidative metabolism during visual stimulation using absolute relaxation rates. *NMR in Biomedicine*, *19*(1), 60–68. https://doi.org/10.1002/nbm.1001

Gagnon, L., Sakad i, S., Lesage, F., Musacchia, J. J., Lefebvre, J., Fang, Q., Yucel, M. A., Evans, K. C., Mandeville, E. T., Cohen-Adad, J., Polimeni, J. R., Yaseen, M. A., Lo, E. H., Greve, D. N., Buxton, R. B., Dale, A. M., Devor, A., & Boas, D. A. (2015). Quantifying the Microvascular Origin of BOLD-fMRI from First Principles with Two-Photon Microscopy

and an Oxygen-Sensitive Nanoprobe. *Journal of Neuroscience*, *35*(8), 3663–3675. https://doi.org/10.1523/JNEUROSCI.3555-14.2015

Garcia, D. M., Duhamel, G., & Alsop, D. C. (2005). Efficiency of inversion pulses for background suppressed arterial spin labeling. *Magnetic Resonance in Medicine*, *54*(2), 366–372. https://doi.org/10.1002/mrm.20556

Gauthier, C. J., Desjardins-Crépeau, L., Madjar, C., Bherer, L., & Hoge, R. D. (2012). Absolute quantification of resting oxygen metabolism and metabolic reactivity during functional activation using QUO2 MRI. *NeuroImage*, *63*(3), 1353–1363. https://doi.org/10.1016/j.neuroimage.2012.07.065

Gauthier, C. J., & Hoge, R. D. (2012). Magnetic resonance imaging of resting OEF and CMRO2 using a generalized calibration model for hypercapnia and hyperoxia. *NeuroImage*, *60*(2), 1212–1225. https://doi.org/10.1016/j.neuroimage.2011.12.056

Germuska, M., Chandler, H. L., Stickland, R. C., Foster, C., Fasano, F., Okell, T. W., Steventon, J., Tomassini, V., Murphy, K., & Wise, R. G. (2019). Dual-calibrated fMRI measurement of absolute cerebral metabolic rate of oxygen consumption and effective oxygen diffusivity. *NeuroImage*, *184*, 717–728. https://doi.org/10.1016/j.neuroimage.2018.09.035

Germuska, M., & Wise, R. G. (2019). Calibrated fMRI for mapping absolute CMRO2: Practicalities and prospects. *NeuroImage*, *187*, 145–153. https://doi.org/10.1016/j.neuroimage.2018.03.068

Gersing, A. S., Ankenbrank, M., Schwaiger, B. J., Toth, V., Janssen, I., Kooijman, H., Wunderlich, S., Bauer, J. S., Zimmer, C., & Preibisch, C. (2015). Mapping of cerebral metabolic rate of oxygen using dynamic susceptibility contrast and blood oxygen level dependent MR imaging in acute ischemic stroke. *Neuroradiology*, *57*(12), 1253–1261. https://doi.org/10.1007/s00234-015-1592-7

Glasser, M. F. (2016). *A multi-modal parcellation of human cerebral cortex*. 11. https://doi.org/10.1038/nature18933

Glasser, M. F., Coalson, T. S., Robinson, E. C., Hacker, C. D., Harwell, J., Yacoub, E., Ugurbil, K., Andersson, J., Beckmann, C. F., Jenkinson, M., Smith, S. M., & Van Essen, D. C. (2016). A multi-modal parcellation of human cerebral cortex. *Nature*, *536*(7615), 171–178. https://doi.org/10.1038/nature18933

Gorgolewski, K., Burns, C. D., Madison, C., Clark, D., Halchenko, Y. O., Waskom, M. L., & Ghosh, S. S. (2011). Nipype: A Flexible, Lightweight and Extensible Neuroimaging Data Processing Framework in Python. *Frontiers in Neuroinformatics*, *5*. https://doi.org/10.3389/fninf.2011.00013

Göttler, J., Kaczmarz, S., Kallmayer, M., Wustrow, I., Eckstein, H.-H., Zimmer, C., Sorg, C., Preibisch, C., & Hyder, F. (2019). Flow-metabolism uncoupling in patients with asymptomatic unilateral carotid artery stenosis assessed by multi-modal magnetic resonance imaging. *Journal of Cerebral Blood Flow & Metabolism*, *39*(11), 2132–2143. https://doi.org/10.1177/0271678X18783369

Grubb, R. L., Raichle, M. E., Eichling, J. O., & Ter-Pogossian, M. M. (1974). The Effects of Changes in Pa CO_2 Cerebral Blood Volume, Blood Flow, and Vascular Mean Transit Time. *Stroke*, *5*(5), 630–639. https://doi.org/10.1161/01.STR.5.5.630

Haacke, E. M., Tang, J., Neelavalli, J., & Cheng, Y. C. N. (2010). Susceptibility mapping as a means to visualize veins and quantify oxygen saturation. *Journal of Magnetic Resonance Imaging*, *32*(3), 663–676. https://doi.org/10.1002/jmri.22276

Hall, C. N., Howarth, C., Kurth-Nelson, Z., & Mishra, A. (2016). Interpreting BOLD: Towards a dialogue between cognitive and cellular neuroscience. *Philosophical Transactions of the Royal Society B: Biological Sciences*, *371*(1705), 20150348. https://doi.org/10.1098/rstb.2015.0348

He, X., & Yablonskiy, D. A. (2007). Quantitative BOLD: Mapping of human cerebral deoxygenated blood volume and oxygen extraction fraction: Default state. *Magnetic Resonance in Medicine*, *57*(1), 115–126. https://doi.org/10.1002/mrm.21108

He, X., Zhu, M., & Yablonskiy, D. A. (2008). Validation of oxygen extraction fraction measurement by qBOLD technique. *Magnetic Resonance in Medicine*, *60*(4), 882–888. https://doi.org/10.1002/mrm.21719

Hedderich, D., Kluge, A., Pyka, T., Zimmer, C., Kirschke, J. S., Wiestler, B., & Preibisch, C. (2019). Consistency of normalized cerebral blood volume values in glioblastoma using different leakage correction algorithms on dynamic susceptibility contrast magnetic resonance imaging data without and with preload. *Journal of Neuroradiology*, *46*(1), 44–51. https://doi.org/10.1016/j.neurad.2018.04.006

Heeger, D. J., Huk, A. C., Geisler, W. S., & Albrecht, D. G. (2000). Spikes versus BOLD: What does neuroimaging tell us about neuronal activity? *Nature Neuroscience*, *3*(7), Article 7. https://doi.org/10.1038/76572

Hillman, E. M. C. (2014). Coupling Mechanism and Significance of the BOLD Signal: A Status Report. *Annual Review of Neuroscience*, *37*(1), 161–181. https://doi.org/10.1146/annurev-neuro-071013-014111

Hirsch, N. M., & Preibisch, C. (2013). T2* Mapping with Background Gradient Correction Using Different Excitation Pulse Shapes. *American Journal of Neuroradiology*, *34*(6), E65–E68. https://doi.org/10.3174/ajnr.A3021

Hirsch, N. M., Toth, V., Förschler, A., Kooijman, H., Zimmer, C., & Preibisch, C. (2014). Technical considerations on the validity of blood oxygenation level-dependent-based MR assessment of vascular deoxygenation: BOLD-BASED ASSESSMENT OF VASCULAR DEOXYGENATION. *NMR in Biomedicine*, *27*(7), 853–862. https://doi.org/10.1002/nbm.3131

Howarth, C., Mishra, A., & Hall, C. N. (2021). More than just summed neuronal activity: How multiple cell types shape the BOLD response. *Philosophical Transactions of the Royal Society B: Biological Sciences*, *376*(1815), 20190630. https://doi.org/10.1098/rstb.2019.0630

Huck, J., Wanner, Y., Fan, A. P., Jäger, A.-T., Grahl, S., Schneider, U., Villringer, A., Steele, C. J., Tardif, C. L., Bazin, P.-L., & Gauthier, C. J. (2019). High resolution atlas of the venous brain vasculature from 7 T quantitative susceptibility maps. *Brain Structure and Function*, *224*(7), 2467–2485. https://doi.org/10.1007/s00429-019-01919-4

Huo, B.-X., Smith, J. B., & Drew, P. J. (2014). Neurovascular coupling and decoupling in the cortex during voluntary locomotion. *The Journal of Neuroscience: The Official Journal of the Society for Neuroscience*, *34*(33), 10975–10981. https://doi.org/10.1523/JNEUROSCI.1369-14.2014

Hyder, D. S. F. (2010). Neurovascular and neurometabolic couplings in dynamic calibrated fMRI: Transient oxidative neuroenergetics for block-design and event-related paradigms. *Frontiers in Neuroenergetics*. https://doi.org/10.3389/fnene.2010.00018

Hyder, D. S. F., Sanganahalli, B., Herman, P., Coman, D., Maandag, N., Behar, K., Blumenfeld, H., & Rothman, D. (2010). Neurovascular and Neurometabolic Couplings in Dynamic

Calibrated fMRI: Transient Oxidative Neuroenergetics for Block-Design and Event-Related Paradigms. *Frontiers in Neuroenergetics*, *2*. https://www.frontiersin.org/articles/10.3389/fnene.2010.00018

Hyder, F., Herman, P., Bailey, C. J., Møller, A., Globinsky, R., Fulbright, R. K., Rothman, D. L., & Gjedde, A. (2016). Uniform distributions of glucose oxidation and oxygen extraction in gray matter of normal human brain: No evidence of regional differences of aerobic glycolysis. *Journal of Cerebral Blood Flow & Metabolism*, *36*(5), 903–916. https://doi.org/10.1177/0271678X15625349

Ino, T., Nakai, R., Azuma, T., Kimura, T., & Fukuyama, H. (2011). Brain Activation During Autobiographical Memory Retrieval with Special Reference to Default Mode Network. *The Open Neuroimaging Journal*, *5*, 14–23. https://doi.org/10.2174/1874440001105010014

Ito, H., Kubo, H., Takahashi, K., Nishijima, K.-I., Ukon, N., Nemoto, A., Sugawara, S., Yamakuni, R., Ibaraki, M., & Ishii, S. (2021). Integrated PET/MRI scanner with oxygen-15 labeled gases for quantification of cerebral blood flow, cerebral blood volume, cerebral oxygen extraction fraction and cerebral metabolic rate of oxygen. *Annals of Nuclear Medicine*, *35*(4), 421–428. https://doi.org/10.1007/s12149-021-01578-8

Jenkinson, M., Beckmann, C. F., Behrens, T. E. J., Woolrich, M. W., & Smith, S. M. (2012). FSL. *NeuroImage*, *62*(2), 782–790. https://doi.org/10.1016/j.neuroimage.2011.09.015

Jiang, D., & Lu, H. (2022). Cerebral oxygen extraction fraction MRI: Techniques and applications. *Magnetic Resonance in Medicine*, *88*(2), 575–600. https://doi.org/10.1002/mrm.29272

Jog, M. A., Yan, L., Kilroy, E., Krasileva, K., Jann, K., LeClair, H., Elashoff, D., & Wang, D. J. J. (2016). Developmental trajectories of cerebral blood flow and oxidative metabolism at baseline and during working memory tasks. *NeuroImage*, *134*, 587–596. https://doi.org/10.1016/j.neuroimage.2016.04.035

Kaczmarz, S., Göttler, J., Petr, J., Hansen, M. B., Mouridsen, K., Zimmer, C., Hyder, F., & Preibisch, C. (2021). Hemodynamic impairments within individual watershed areas in asymptomatic carotid artery stenosis by multimodal MRI. *Journal of Cerebral Blood Flow & Metabolism*, *41*(2), 380–396. https://doi.org/10.1177/0271678X20912364

Kaczmarz, S., Göttler, J., Zimmer, C., Hyder, F., & Preibisch, C. (2020). Characterizing white matter fiber orientation effects on multi-parametric quantitative BOLD assessment of oxygen extraction fraction. *Journal of Cerebral Blood Flow & Metabolism*, *40*(4), 760–774. https://doi.org/10.1177/0271678X19839502

Kaczmarz, S., Hyder, F., & Preibisch, C. (2020). Oxygen extraction fraction mapping with multi-parametric quantitative BOLD MRI: Reduced transverse relaxation bias using 3D-GraSE imaging. *NeuroImage*, *220*, 117095. https://doi.org/10.1016/j.neuroimage.2020.117095

Kim, J., Whyte, J., Wang, J., Rao, H., Tang, K. Z., & Detre, J. A. (2006). Continuous ASL perfusion fMRI investigation of higher cognition: Quantification of tonic CBF changes during sustained attention and working memory tasks. *NeuroImage*, *31*(1), 376–385. https://doi.org/10.1016/j.neuroimage.2005.11.035

Kim, S.-G., & Ogawa, S. (2012). Biophysical and Physiological Origins of Blood Oxygenation Level-Dependent fMRI Signals. *Journal of Cerebral Blood Flow & Metabolism*, *32*(7), 1188–1206. https://doi.org/10.1038/jcbfm.2012.23

Kluge, A., Lukas, M., Toth, V., Pyka, T., Zimmer, C., & Preibisch, C. (2016). Analysis of three leakage-correction methods for DSC-based measurement of relative cerebral blood volume with respect to heterogeneity in human gliomas. *Magnetic Resonance Imaging*, *34*(4), 410–421. https://doi.org/10.1016/j.mri.2015.12.015

Koush, Y., de Graaf, R. A., Kupers, R., Dricot, L., Ptito, M., Behar, K. L., Rothman, D. L., & Hyder, F. (2021). Metabolic underpinnings of activated and deactivated cortical areas in human brain. *Journal of Cerebral Blood Flow & Metabolism*, *41*(5), 986–1000. https://doi.org/10.1177/0271678X21989186

Krishnan, A., Williams, L. J., McIntosh, A. R., & Abdi, H. (2011). Partial Least Squares (PLS) methods for neuroimaging: A tutorial and review. *NeuroImage*, *56*(2), 455–475. https://doi.org/10.1016/j.neuroimage.2010.07.034

Kufer, J., Preibisch, C., Epp, S., Göttler, J., Schmitzer, L., Zimmer, C., Hyder, F., & Kaczmarz, S. (2022). Imaging effective oxygen diffusivity in the human brain with multiparametric magnetic resonance imaging. *Journal of Cerebral Blood Flow & Metabolism*, *42*(2), 349–363. https://doi.org/10.1177/0271678X211048412

Lee, H., & Wehrli, F. W. (2022). Whole-brain 3D mapping of oxygen metabolism using constrained quantitative BOLD. *NeuroImage*, *250*, 118952. https://doi.org/10.1016/j.neuroimage.2022.118952

Leenders, K. L., Perani, D., Lammertsma, A. A., Heather, J. D., Buckingham, P., Jones, T., Healy, M. J. R., Gibbs, J. M., Wise, R. J. S., Hatazawa, J., Herold, S., Beaney, R. P., Brooks, D. J., Spinks, T., Rhodes, C., & Frackowiak, R. S. J. (1990). CEREBRAL BLOOD FLOW, BLOOD VOLUME AND OXYGEN UTILIZATION: NORMAL VALUES AND EFFECT OF AGE. *Brain*, *113*(1), 27–47. https://doi.org/10.1093/brain/113.1.27

Leithner, C., & Royl, G. (2014). The Oxygen Paradox of Neurovascular Coupling. *Journal of Cerebral Blood Flow & Metabolism*, *34*(1), 19–29. https://doi.org/10.1038/jcbfm.2013.181

Leithner, C., Royl, G., Offenhauser, N., Füchtemeier, M., Kohl-Bareis, M., Villringer, A., Dirnagl, U., & Lindauer, U. (2010). Pharmacological Uncoupling of Activation Induced Increases in CBF and $CMRO_2$. *Journal of Cerebral Blood Flow & Metabolism*, *30*(2), 311–322. https://doi.org/10.1038/jcbfm.2009.211

Leontiev, O., & Buxton, R. B. (2007). Reproducibility of BOLD, perfusion, and CMRO2 measurements with calibrated-BOLD fMRI. *NeuroImage*, *35*(1), 175–184. https://doi.org/10.1016/j.neuroimage.2006.10.044

Liang, X., Zou, Q., He, Y., & Yang, Y. (2013). Coupling of functional connectivity and regional cerebral blood flow reveals a physiological basis for network hubs of the human brain. *Proceedings of the National Academy of Sciences*, *110*(5), 1929–1934. https://doi.org/10.1073/pnas.1214900110

Lin, P., Hasson, U., Jovicich, J., & Robinson, S. (2011a). A Neuronal Basis for Task-Negative Responses in the Human Brain. *Cerebral Cortex*, *21*(4), 821–830. https://doi.org/10.1093/cercor/bhq151

Lin, P., Hasson, U., Jovicich, J., & Robinson, S. (2011b). A Neuronal Basis for Task-Negative Responses in the Human Brain. *Cerebral Cortex*, *21*(4), 821–830. https://doi.org/10.1093/cercor/bhq151

Logothetis, N. K., Pauls, J., Augath, M., Trinath, T., & Oeltermann, A. (2001). Neurophysiological investigation of the basis of the fMRI signal. *Nature*, *412*(6843), Article 6843. https://doi.org/10.1038/35084005

Lüsebrink, F., Mattern, H., Yakupov, R., Acosta-Cabronero, J., Ashtarayeh, M., Oeltze-Jafra, S., & Speck, O. (2021). Comprehensive ultrahigh resolution whole brain in vivo MRI dataset as a human phantom. *Scientific Data*, *8*(1), 138. https://doi.org/10.1038/s41597-021-00923-w

Ma, Y., Sun, H., Cho, J., Mazerolle, E. L., Wang, Y., & Pike, G. B. (2020). Cerebral OEF quantification: A comparison study between quantitative susceptibility mapping and dual-gas calibrated BOLD imaging. *Magnetic Resonance in Medicine*, *83*(1), 68–82. https://doi.org/10.1002/mrm.27907

Maralani, P. J., Das, S., Mainprize, T., Phan, N., Bharatha, A., Keith, J., Munoz, D. G., Sahgal, A., Symons, S., Ironside, S., Faraji-Dana, Z., Eilaghi, A., Chan, A., Alcaide-Leon, P., Shearkhani, O., Jakubovic, R., Atenafu, E. G., Zaharchuk, G., & Mikulis, D. (2018). Hypoxia Detection in Infiltrative Astrocytoma: Ferumoxytol-based Quantitative BOLD MRI with Intraoperative and Histologic Validation. *Radiology*, *288*(3), 821–829. https://doi.org/10.1148/radiol.2018172601

Martínez-Maestro, M., Labadie, C., & Möller, H. E. (2019). Dynamic metabolic changes in human visual cortex in regions with positive and negative blood oxygenation level-dependent response. *Journal of Cerebral Blood Flow & Metabolism*, *39*(11), 2295–2307. https://doi.org/10.1177/0271678X18795426

McIntosh, A. R., & Lobaugh, N. J. (2004). Partial least squares analysis of neuroimaging data: Applications and advances. *NeuroImage*, *23*, S250–S263. https://doi.org/10.1016/j.neuroimage.2004.07.020

McIntosh, A. R., & Mišić, B. (2013). Multivariate Statistical Analyses for Neuroimaging Data. *Annual Review of Psychology*, *64*(1), 499–525. https://doi.org/10.1146/annurev-psych-113011-143804

Mullinger, K. J., Mayhew, S. D., Bagshaw, A. P., Bowtell, R., & Francis, S. T. (2014). Evidence that the negative BOLD response is neuronal in origin: A simultaneous EEG–BOLD–CBF study in humans. *NeuroImage*, *94*, 263–274. https://doi.org/10.1016/j.neuroimage.2014.02.029

Mutsaerts, H. J. M. M., Steketee, R. M. E., Heijtel, D. F. R., Kuijer, J. P. A., van Osch, M. J. P., Majoie, C. B. L. M., Smits, M., & Nederveen, A. J. (2014). Inter-Vendor Reproducibility of Pseudo-Continuous Arterial Spin Labeling at 3 Tesla. *PLoS ONE*, *9*(8), e104108. https://doi.org/10.1371/journal.pone.0104108

Nagaoka, T., Zhao, F., Wang, P., Harel, N., Kennan, R. P., Ogawa, S., & Kim, S.-G. (2006). Increases in Oxygen Consumption without Cerebral Blood Volume Change during Visual Stimulation under Hypotension Condition. *Journal of Cerebral Blood Flow & Metabolism*, *26*(8), 1043–1051. https://doi.org/10.1038/sj.jcbfm.9600251

Nöth, U., Volz, S., Hattingen, E., & Deichmann, R. (2014). An improved method for retrospective motion correction in quantitative T2* mapping. *NeuroImage*, *92*, 106–119. https://doi.org/10.1016/j.neuroimage.2014.01.050

Notter, M., Gale, D., Herholz, P., Markello, R., Notter-Bielser, M.-L., & Whitaker, K. (2019). AtlasReader: A Python package to generate coordinate tables, region labels, and informative figures from statistical MRI images. *Journal of Open Source Software*, *4*(34), 1257. https://doi.org/10.21105/joss.01257

Pasley, B. N., Inglis, B. A., & Freeman, R. D. (2007). Analysis of oxygen metabolism implies a neural origin for the negative BOLD response in human visual cortex. *NeuroImage*, *36*(2), 269–276. https://doi.org/10.1016/j.neuroimage.2006.09.015

Pfefferbaum, A., Chanraud, S., Pitel, A.-L., Muller-Oehring, E., Shankaranarayanan, A., Alsop, D. C., Rohlfing, T., & Sullivan, E. V. (2011). Cerebral Blood Flow in Posterior Cortical Nodes of the Default Mode Network Decreases with Task Engagement but Remains Higher than in Most Brain Regions. *Cerebral Cortex*, *21*(1), 233–244. https://doi.org/10.1093/cercor/bhq090

Phillips, A. A., Chan, F. H., Zheng, M. M. Z., Krassioukov, A. V., & Ainslie, P. N. (2016). Neurovascular coupling in humans: Physiology, methodological advances and clinical implications. *Journal of Cerebral Blood Flow & Metabolism*, *36*(4), 647–664. https://doi.org/10.1177/0271678X15617954

Preibisch, C., Shi, K., Kluge, A., Lukas, M., Wiestler, B., Göttler, J., Gempt, J., Ringel, F., Al Jaberi, M., Schlegel, J., Meyer, B., Zimmer, C., Pyka, T., & Förster, S. (2017). Characterizing hypoxia in human glioma: A simultaneous multimodal MRI and PET study. *NMR in Biomedicine*, *30*(11), e3775. https://doi.org/10.1002/nbm.3775

Preibisch, C., Volz, S., Anti, S., & Deichmann, R. (2008). Exponential excitation pulses for improved water content mapping in the presence of background gradients. *Magnetic Resonance in Medicine*, *60*(4), 908–916. https://doi.org/10.1002/mrm.21730

Qihong Zou, Yihong Yang, Jia-Hong Gao, Hong Gu, & Danny J.J. Wang. (2011). Quantification of Load Dependent Brain Activity in Parametric N-Back Working Memory Tasks using Pseudo-continuous Arterial Spin Labeling (pCASL) Perfusion Imaging. *Journal of Cognitive Science*, *12*(2), 129–149. https://doi.org/10.17791/jcs.2011.12.2.129

Raichle, M. E., MacLeod, A. M., Snyder, A. Z., Powers, W. J., Gusnard, D. A., & Shulman, G. L. (2001). A default mode of brain function. *Proceedings of the National Academy of Sciences*, *98*(2), 676–682. https://doi.org/10.1073/pnas.98.2.676

Rees, G., Friston, K., & Koch, C. (2000). A direct quantitative relationship between the functional properties of human and macaque V5. *Nature Neuroscience*, *3*(7), 716–723. https://doi.org/10.1038/76673

Restom, K., Perthen, J. E., & Liu, T. T. (2008). Calibrated fMRI in the medial temporal lobe during a memory-encoding task. *NeuroImage*, *40*(4), 1495–1502. https://doi.org/10.1016/j.neuroimage.2008.01.038

Rossetti, G. M., d'Avossa, G., Rogan, M., Macdonald, J. H., Oliver, S. J., & Mullins, P. G. (2021). Reversal of neurovascular coupling in the default mode network: Evidence from hypoxia. *Journal of Cerebral Blood Flow & Metabolism*, *41*(4), 805–818. https://doi.org/10.1177/0271678X20930827

Roy, R. K., Althammer, F., Seymour, A. J., Du, W., Biancardi, V. C., Hamm, J. P., Filosa, J. A., Brown, C. H., & Stern, J. E. (2021). Inverse neurovascular coupling contributes to positive feedback excitation of vasopressin neurons during a systemic homeostatic challenge. *Cell Reports*, *37*(5), 109925. https://doi.org/10.1016/j.celrep.2021.109925

Sanganahalli, B. G., Herman, P., Rothman, D. L., Blumenfeld, H., & Hyder, F. (2016). Metabolic demands of neural-hemodynamic associated and disassociated areas in brain. *Journal of Cerebral Blood Flow & Metabolism*, *36*(10), 0271678X16664531. https://doi.org/10.1177/0271678X16664531

Schridde, U., Khubchandani, M., Motelow, J. E., Sanganahalli, B. G., Hyder, F., & Blumenfeld, H. (2008). Negative BOLD with Large Increases in Neuronal Activity. *Cerebral Cortex*, *18*(8), 1814–1827. https://doi.org/10.1093/cercor/bhm208

Shaw, K., Bell, L., Boyd, K., Grijseels, D. M., Clarke, D., Bonnar, O., Crombag, H. S., & Hall, C. N. (2021). Neurovascular coupling and oxygenation are decreased in hippocampus

compared to neocortex because of microvascular differences. *Nature Communications*, *12*(1), 3190. https://doi.org/10.1038/s41467-021-23508-y

Shih, Y.-Y. I., Wey, H.-Y., De La Garza, B. H., & Duong, T. Q. (2011). Striatal and Cortical BOLD, Blood Flow, Blood Volume, Oxygen Consumption, and Glucose Consumption Changes in Noxious Forepaw Electrical Stimulation. *Journal of Cerebral Blood Flow & Metabolism*, *31*(3), 832–841. https://doi.org/10.1038/jcbfm.2010.173

Shmuel, A., Augath, M., Oeltermann, A., & Logothetis, N. K. (2006). Negative functional MRI response correlates with decreases in neuronal activity in monkey visual area V1. *Nature Neuroscience*, *9*(4), 569–577. https://doi.org/10.1038/nn1675

Shmuel, A., Yacoub, E., Pfeuffer, J., Van de Moortele, P.-F., Adriany, G., Hu, X., & Ugurbil, K. (2002). Sustained Negative BOLD, Blood Flow and Oxygen Consumption Response and Its Coupling to the Positive Response in the Human Brain. *Neuron*, *36*(6), 1195–1210. https://doi.org/10.1016/S0896-6273(02)01061-9

Shulman, G. L., Corbetta, M., Buckner, R. L., Fiez, J. A., Miezin, F. M., Raichle, M. E., & Petersen, S. E. (1997). Common Blood Flow Changes across Visual Tasks: I. Increases in Subcortical Structures and Cerebellum but Not in Nonvisual Cortex. *Journal of Cognitive Neuroscience*, *9*(5), 624–647. https://doi.org/10.1162/jocn.1997.9.5.624

Shulman, G. L., FIEZ, J. A., Corbetta, M., Buckner, R. L., Miezin, F. M., Raichle, M. E., & Petersen, S. E. (1997). Common Blood Flow Changes across Visual Tasks: II. Decreases in Cerebral Cortex. *Journal of cognitive neuroscience*, *9*(5), 648–663. https://doi.org/10.1162/jocn.1997.9.5.648

Siero, J. C., Hermes, D., Hoogduin, H., Luijten, P. R., Petridou, N., & Ramsey, N. F. (2013). BOLD Consistently Matches Electrophysiology in Human Sensorimotor Cortex at Increasing Movement Rates: A Combined 7T fMRI and ECoG Study on Neurovascular Coupling. *Journal of Cerebral Blood Flow & Metabolism*, *33*(9), 1448–1456. https://doi.org/10.1038/jcbfm.2013.97

Singh, K. D., & Fawcett, I. P. (2008). Transient and linearly graded deactivation of the human default-mode network by a visual detection task. *NeuroImage*, *41*(1), 100–112. https://doi.org/10.1016/j.neuroimage.2008.01.051

Sirotin, Y. B., & Das, A. (2009). Anticipatory haemodynamic signals in sensory cortex not predicted by local neuronal activity. *Nature*, *457*(7228), 475–479. https://doi.org/10.1038/nature07664

Smallwood, J., Bernhardt, B. C., Leech, R., Bzdok, D., Jefferies, E., & Margulies, D. S. (2021). The default mode network in cognition: A topographical perspective. *Nature Reviews Neuroscience*, *22*(8), 503–513. https://doi.org/10.1038/s41583-021-00474-4

Smith, S. M., Jenkinson, M., Woolrich, M. W., Beckmann, C. F., Behrens, T. E. J., Johansen-Berg, H., Bannister, P. R., De Luca, M., Drobnjak, I., Flitney, D. E., Niazy, R. K., Saunders, J., Vickers, J., Zhang, Y., De Stefano, N., Brady, J. M., & Matthews, P. M. (2004). Advances in functional and structural MR image analysis and implementation as FSL. *NeuroImage*, *23*, S208–S219. https://doi.org/10.1016/j.neuroimage.2004.07.051

Spreng, R. N., & Grady, C. L. (2010). Patterns of Brain Activity Supporting Autobiographical Memory, Prospection, and Theory of Mind, and Their Relationship to the Default Mode Network. *Journal of Cognitive Neuroscience*, *22*(6), 1112–1123. https://doi.org/10.1162/jocn.2009.21282

Spreng, R. N., Stevens, W. D., Chamberlain, J. P., Gilmore, A. W., & Schacter, D. L. (2010). Default network activity, coupled with the frontoparietal control network, supports

goal-directed cognition. *NeuroImage*, *53*(1), 303–317. https://doi.org/10.1016/j.neuroimage.2010.06.016

Stadlbauer, A., Zimmermann, M., Kitzwögerer, M., Oberndorfer, S., Rössler, K., Dörfler, A., Buchfelder, M., & Heinz, G. (2017). MR Imaging–derived Oxygen Metabolism and Neovascularization Characterization for Grading and *IDH* Gene Mutation Detection of Gliomas. *Radiology*, *283*(3), 799–809. https://doi.org/10.1148/radiol.2016161422

Stefanovic, B., Warnking, J. M., & Pike, G. B. (2004). Hemodynamic and metabolic responses to neuronal inhibition. *NeuroImage*, *22*(2), 771–778. https://doi.org/10.1016/j.neuroimage.2004.01.036

Stiernman, L. J., Grill, F., Hahn, A., Rischka, L., Lanzenberger, R., Panes Lundmark, V., Riklund, K., Axelsson, J., & Rieckmann, A. (2021). Dissociations between glucose metabolism and blood oxygenation in the human default mode network revealed by simultaneous PET-fMRI. *Proceedings of the National Academy of Sciences*, *118*(27), e2021913118. https://doi.org/10.1073/pnas.2021913118

Stone, A. J., & Blockley, N. P. (2017a). A streamlined acquisition for mapping baseline brain oxygenation using quantitative BOLD. *NeuroImage*, *147*, 79–88. https://doi.org/10.1016/j.neuroimage.2016.11.057

Stone, A. J., & Blockley, N. P. (2017b). A streamlined acquisition for mapping baseline brain oxygenation using quantitative BOLD. *NeuroImage*, *147*, 79–88. https://doi.org/10.1016/j.neuroimage.2016.11.057

Takata, N., Sugiura, Y., Yoshida, K., Koizumi, M., Hiroshi, N., Honda, K., Yano, R., Komaki, Y., Matsui, K., Suematsu, M., Mimura, M., Okano, H., & Tanaka, K. F. (2018). Optogenetic astrocyte activation evokes BOLD fMRI response with oxygen consumption without neuronal activity modulation. *Glia*, *66*(9), 2013–2023. https://doi.org/10.1002/glia.23454

Thomas Yeo, B. T., Krienen, F. M., Sepulcre, J., Sabuncu, M. R., Lashkari, D., Hollinshead, M., Roffman, J. L., Smoller, J. W., Zöllei, L., Polimeni, J. R., Fischl, B., Liu, H., & Buckner, R. L. (2011). The organization of the human cerebral cortex estimated by intrinsic functional connectivity. *Journal of Neurophysiology*, *106*(3), 1125–1165. https://doi.org/10.1152/jn.00338.2011

Tóth, V., Förschler, A., Hirsch, N. M., Den Hollander, J., Kooijman, H., Gempt, J., Ringel, F., Schlegel, J., Zimmer, C., & Preibisch, C. (2013). MR-based hypoxia measures in human glioma. *Journal of Neuro-Oncology*, *115*(2), 197–207. https://doi.org/10.1007/s11060-013-1210-7

Tsvetanov, K. A., Henson, R. N. A., & Rowe, J. B. (2020). Separating vascular and neuronal effects of age on fMRI BOLD signals. *Philosophical Transactions of the Royal Society B: Biological Sciences*, *376*(1815), 20190631. https://doi.org/10.1098/rstb.2019.0631

Uhlirova, H., Kılıç, K., Tian, P., Thunemann, M., Desjardins, M., Saisan, P. A., Sakadžić, S., Ness, T. V., Mateo, C., Cheng, Q., Weldy, K. L., Razoux, F., Vandenberghe, M., Cremonesi, J. A., Ferri, C. G., Nizar, K., Sridhar, V. B., Steed, T. C., Abashin, M., … Devor, A. (2016). Cell type specificity of neurovascular coupling in cerebral cortex. *eLife*, *5*, e14315. https://doi.org/10.7554/eLife.14315

Uludağ, K., Dubowitz, D. J., Yoder, E. J., Restom, K., Liu, T. T., & Buxton, R. B. (2004). Coupling of cerebral blood flow and oxygen consumption during physiological activation and deactivation measured with fMRI. *NeuroImage*, *23*(1), 148–155. https://doi.org/10.1016/j.neuroimage.2004.05.013

Vanzetta, I., & Grinvald, A. (1999). Increased Cortical Oxidative Metabolism Due to Sensory Stimulation: Implications for Functional Brain Imaging. *Science*, *286*(5444), 1555–1558. https://doi.org/10.1126/science.286.5444.1555

Waskom, M. (2021). seaborn: Statistical data visualization. *Journal of Open Source Software*, *6*(60), 3021. https://doi.org/10.21105/joss.03021

Wiestler, B., Kluge, A., Lukas, M., Gempt, J., Ringel, F., Schlegel, J., Meyer, B., Zimmer, C., Förster, S., Pyka, T., & Preibisch, C. (2016). Multiparametric MRI-based differentiation of WHO grade II/III glioma and WHO grade IV glioblastoma. *Scientific Reports*, *6*(1), 35142. https://doi.org/10.1038/srep35142

Wilson, R., Mullinger, K. J., Francis, S. T., & Mayhew, S. D. (2019). The relationship between negative BOLD responses and ERS and ERD of alpha/beta oscillations in visual and motor cortex. *NeuroImage*, *199*, 635–650. https://doi.org/10.1016/j.neuroimage.2019.06.009

Wise, R. G., Harris, A. D., Stone, A. J., & Murphy, K. (2013). Measurement of OEF and absolute CMRO2: MRI-based methods using interleaved and combined hypercapnia and hyperoxia. *NeuroImage*, *83*, 135–147. https://doi.org/10.1016/j.neuroimage.2013.06.008

Xu, B., Liu, T., Spincemaille, P., Prince, M., & Wang, Y. (2014). Flow compensated quantitative susceptibility mapping for venous oxygenation imaging. *Magnetic Resonance in Medicine*, *72*(2), 438–445. https://doi.org/10.1002/mrm.24937

Yablonskiy, D. A., & Haacke, E. M. (1994). Theory of NMR signal behavior in magnetically inhomogeneous tissues: The static dephasing regime. *Magnetic Resonance in Medicine*, *32*(6), 749–763. https://doi.org/10.1002/mrm.1910320610

Zaldivar, D., Rauch, A., Whittingstall, K., Logothetis, N. K., & Goense, J. (2014). Dopamine-Induced Dissociation of BOLD and Neural Activity in Macaque Visual Cortex. *Current Biology*, *24*(23), 2805–2811. https://doi.org/10.1016/j.cub.2014.10.006

Zhang, J., Liu, T., Gupta, A., Spincemaille, P., Nguyen, T. D., & Wang, Y. (2015). Quantitative mapping of cerebral metabolic rate of oxygen ($CMRO_2$) using quantitative susceptibility mapping (QSM): Quantitative $CMRO_2$ Mapping Using QSM. *Magnetic Resonance in Medicine*, *74*(4), 945–952. https://doi.org/10.1002/mrm.25463

Zhang, Y., Du, W., Yin, Y., Li, H., Liu, Z., Yang, Y., Han, Y., & Gao, J.-H. (2021). Impaired cerebral vascular and metabolic responses to parametric N-back tasks in subjective cognitive decline. *Journal of Cerebral Blood Flow & Metabolism*, *41*(10), 2743–2755. https://doi.org/10.1177/0271678X211012153